The Hong Kong Polytechnic University
Department of Applied Physics

Heteroepitaxy and Characterization of Perovskite Titanate Thin Films Grown on III-V Semiconductor

YANG Zhibin

A thesis submitted in partial fulfillment of the requirements
for the degree of Master of Philosophy

October 2012

CERTIFICATE OF ORIGINALITY

I hereby declare that this thesis is my own work and that, to the best of my knowledge and belief, it reproduces no material previously published or written, nor material that has been accepted for the award of any other degree or diploma, except where due acknowledgement has been made in the text.

______________________________________ (Signed)

__________YANG Zhibin__________ (Name of student)

ABSTRACT

In recent years, the integration of perovskite titanates with mature semiconductor technology has attracted extensive attention for both basic research and applications. Perovskite titanates such as (Ba, Sr)TiO_3 (BST) have relatively high dielectric tunability and moderate dielectric constant, which have found many applications for frequency and phase agile microwave devices. Up to now, the titanate-based tunable devices have been well fabricated on single-crystal oxide substrates such as MgO and $LaAlO_3$. III–V semiconductors such as GaAs have direct band gap and higher saturated electron mobility compared to conventional silicon (Si), making them very suitable for high-speed microelectronic and photonic devices. Hence, it is of great interest to combine ferroelectric titanates with GaAs exhibiting high-performance microwave capabilities.

In the present thesis, ferroelectric BST thin films were epitaxially grown on GaAs (001) substrate using $SrTiO_3$ (STO) as a buffer layer by laser molecular beam epitaxy. The STO buffer layer was first deposited on GaAs substrate by setting the substrate temperature around 600 °C and the pressure of 5×10^{-5} Pa. During the BST thin film deposition, the substrate temperature was maintained at 620 °C and the oxygen partial pressure was kept at 1 Pa. After deposition, the heterostructure was annealed in 200 Pa oxygen pressure for 1 hr to reduce oxygen vacancies. X-ray diffraction measurements indicate that BST is well crystallized and epitaxially aligned with STO/GaAs. Atomic force microscope studies show that the films have atomically flat surfaces. The interface structure of STO/GaAs was studied by transmission electron microscopy (TEM). The sharp interface from TEM image provides an evidence that the STO film deposited on GaAs has good crystallinity. The chemical valences of BST thin films on STO/GaAs and energy band at the interface of STO/GaAs were investigated using photoelectron spectroscopy. A type II heterojunction with a valence band offset of 2.5 eV and conduction band offset of 0.7 eV is formed.

The dielectric and ferroelectric properties of BST/STO/GaAs heterostructure are studied. The measurements were conducted by applying coplanar configurations on BST thin films. With increasing frequency from 100 kHz to 10 MHz, the dielectric constant of the film was reduced from 870 to 700 accordingly. The in-plane dielectric properties of the heteroepitaxial structure under different applying frequency were investigated from -190 to 90 °C, indicating Curie temperature of the BST film to be around 52 °C. At room temperature, the dielectric constant of the heterostructure under moderate dc bias field can be tuned by 30% and *K* factor is found to be close to 8. By considering the high-frequency capabilities and large-size availability of commercial GaAs, this work shows that the BST/STO/GaAs heterostructure can be processed to be a new system for tunable microwave applications.

LIST OF PUBLICATIONS

1. Z. B. Yang and J. H. Hao, "In-plane dielectric properties of epitaxial $Ba_{0.7}Sr_{0.3}TiO_3$ thin films grown on GaAs for tunable device application", *Journal of Applied Physics*, **112**, 054110 (2012).

2. X. H. Wei, W. Huang, Z. B. Yang and J. H. Hao, "Interfacial and rectifying characteristic of epitaxial $SrTiO_{3-\delta}$/GaAs *p-n* junctions", *Scripta Materialia*, **65,** 323 (2011).

3. Z. B. Yang, G. Y. Gao and J. H. Hao, "Heteroepitaxy and characterization of perovskite titanate thin films grown on III-V semiconductor", *International Symposium on Integrated Functionalities* (ISIF 2012), Hong Kong China, June 18-21, 2012. (Abstract Page 166).

4. Z. B. Yang and J. H. Hao, "Band alignment of epitaxial perovskite titanate thin films grown on GaAs substrates by laser molecular beam epitaxy" (tentative title), to be submitted.

5. G. Y. Gao, Z. B. Yang, Y. Wang, H. L. W. Chan, W. B. Wu and J. H. Hao, “Growth and multiferroic properties of Mn-doped $BiFeO_3$ films epitaxially on $SrTiO_3$ buffered GaAs”, (tentative title), to be submitted.

ACKNOWLEDGEMENTS

First and foremost, I would like to acknowledge the support from my supervisor, Dr. J. H. Hao for his valuable guidance and brilliant supervision throughout the period of my postgraduate study. I would also like to thank Prof. H. L. W. Chan, Prof. C. L. Choy, Dr. J. Y. Dai, Dr. F. Yan and Dr. Y. Wang for their assistance on my research and coursework studies.

I would like to thank Dr. G. Y. Gao, Dr. X. H. Wei, Dr. W. Huang for providing invaluable supports and suggestions to this work.

I would like to give thanks to Mr. M. N. Yeung of the Materials Research Centre for his assistance in the structure characterization.

I am gratefully to all my friends and colleagues in AP for their help and assistance. They include Dr. Y. Zhang, Mr. F. Tong, Miss W. J. Jie, Mr. M. K. Tsang, and Mr. K. W. Mak.

I gratefully acknowledge the financial support from the Research Grants Council of Hong Kong (GRF No. PolyU 500910).

Finally, I would like to express my deepest appreciations to my parents for their support, encouragement and enduring love over the years. Without you this would not have been possible.

TABLE OF CONTENTS

LIST OF FIGURE CAPTIONS

LIST OF TABLE CAPTIONS

LIST OF SYMBOLS

Symbol	**Description**
r	radius
ε	relative permittivity
C	Curie constant
T_0	Curie-Weiss temperature
T_c	Curie temperature
E	electric field
P_r	remnant polarization
ε'	the real part of the permittivity
ε''	the imaginary component of the permittivity
$tan\delta$	the loss tangent
K	figure of merit
$\varepsilon(T, E)$	the dielectric constant under the electrical field
$\varepsilon(T, 0)$	the dielectric constant under zero field

LIST OF ACRONYMS

Acronyms	**Description**
AFM	Atomic force microscopy
BST	Barium strontium titanate, (Ba, Sr)TiO_3
FWHM	Full width at half maximum
LMBE	Laser molecular beam epitaxy
MBE	Molecular beam epitaxy
PLD	Pulsed laser deposition
RF	Radio frequency
RHEED	Reflection high energy electron diffraction
rms	Root mean square
TEM	Transmission electron microscopy
STO	Strontium titanate, $SrTiO_3$
UHV	Ultra-high vacuum
UPS	Ultraviolet photoemission spectroscopy
XPS	X-ray photoemission spectroscopy
XRD	X-ray diffractions

CHAPTER 1

Introduction and literature review

1.1 Introduction to perovskite titanate

1.1.1 Structure of perovskite titanate

After barium titanate ($BaTiO_3$, abbreviated as BTO) was discovered in 1949, the perovskite family became very attractive for both applications and basic research. Typical materials of this family include BTO, $PbTiO_3$, $Pb(Mn_{1/3}Nb_{2/3})O_3$ and etc, which have found potential applications in electronic, electro-optical, and electromechanical fields. On the other hand, perovskite materials are quite attractive for the basic research due to perovskites have a relatively simple structure and can show different phases when its minor composition changes.

Perovskite is the mineral name for calcium titanium oxide ($CaTiO_3$), and is used to designate the structure with formula of ABO_3. In 1839, a Russian mineralogist discovered a new mineral $CaTiO_3$ and he named it to perovskite. This name has since been used for the large ABO_3 family.

As shown in Fig. 1.1, in the perovskite structure, *A* represents a divalent, and *B* is represents a tetravalent. In the ideal structure, large *A* atoms located at the corners of the cubic cell, the smaller *B* atoms being placed in the centre and the oxygen atoms are located in the centre of each cubic face. The crystal structure of an ideal perovskite can be described as a face centered cubic lattice structure with each *A* atoms surrounded by 12 equidistant oxygen ions and each B atoms in the center of an octahedron composed of oxygen ions.

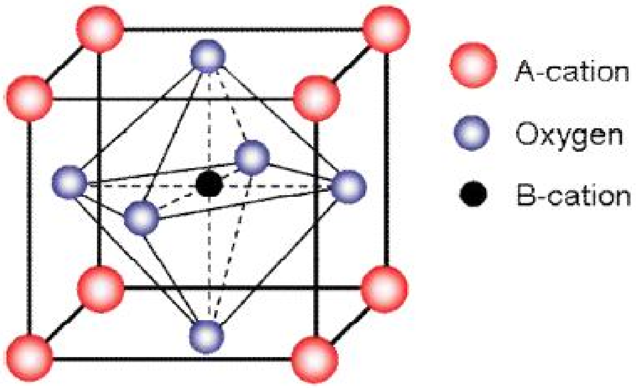

Fig. 1.1 The lattice structure of the ABO_3 ideal cubic perovskite [Moulson and Herbert, 2003].

Only some of the perovskites can show this ideal structure, for instance, $SrTiO_3$ (STO) at room temperature. In general, the structure is modified by cation displacements as in BTO or by tilting of octahedra as in $CaTiO_3$ or by a combination of both as in $NaNbO_3$ [Glazer, 1972]. Goldschmidt present a new model for the perovskite structure at the early 1920s. Ionic radius is one of the basic principles of the model. By the way, it also follows that when the anions contact with the cations, the anions should surround with the cations. And the sum of anions and cations ionic radius is setting to be the distance between them. For a perfect perovskite structure, the relationship between ionic radii can be measured by a tolerance factor (t) as given is Equation 1.1, i. e.:

$$t = \frac{R_A + R_O}{\sqrt{2} \cdot (R_B + R_O)} \tag{1.1}$$

where R_A, R_B and R_O represent ionic radii of A, B and O atoms respectively for studying the stability quality of perovskite [Feng et al., 2008, Li et al., 2004]. t is 1.0 for an perfect perovskite structure. However, for most cubic perovskites, the t value is between 0.8 and 0.9, and for distorted perovskites, t values have smaller values but wider range. Nevertheless, for some systems whose t is within the most favored range (0.8 - 0.9), a perovskite structure is not stable [Feng et al., 2008]. It seems that the t is a necessary but not sufficient condition for perovskite formation. An octahedral factor (μ) has therefore also been introduced to predict perovskite stability, defined as:

$$\mu = \frac{R_B}{R_O} \tag{1.2}$$

According to the literature review, the highest and lowest values of μ are 0.6785 [Feng et al., 2008] and 0.425 [Li et al., 2004], respectively. For the perovskite structure, the BO_6 octahedron is the most important basic unit, which will be unstable with a small B-cation. Then, perovskite structure cannot be formed. The formation of perovskite structure can be predicted by using both the tolerance factor and the octahedral factor [Li et al., 2004].

1.1.2 Structural phase transitions

In 1943, BTO was discovered to have a high dielectric constant of 1200-1500 and it has been a subject of interest for numerous researchers and now has many applications [Richerson, 2006]. At high temperatures, BTO has the ideal cubic unit cell shown in Fig. 1.1, the oxygen ions and barium ions together forming a face centered cubic lattice with each barium ion surrounded by 12 oxygen ions. Each titanium atoms are located in internal positions of oxygen-cornered octahedron. At low temperatures, the titanium ions are too small to be stable in their octahedral interstitial positions and they randomly move off-centre in the direction of any of the six oxygen ions surrounding them to achieve a minimum energy configuration [Richerson, 2006]. All ferroelectric materials have a transition temperature, the Curie point (T_C), such that at a temperature $T > T_C$ the crystal does not exhibit ferroelectricity, while for $T < T_C$ it is ferroelectric [Damjanovic, 1998]. For materials have two or more ferroelectric states, a second transition temperature can be defined as the temperature at which the crystal transforms from one ferroelectric phase to another [Damjanovic, 1998]. As shown in Fig. 1.2, the crystal structure and polarization characteristics of BTO are strongly dependent on temperature and in regions close to each transition temperature, thermodynamic, dielectric, elastic, optical and thermal properties all show anomalous behavior [Lines and Glass, 1979 cited in Damjanovic, 1998].

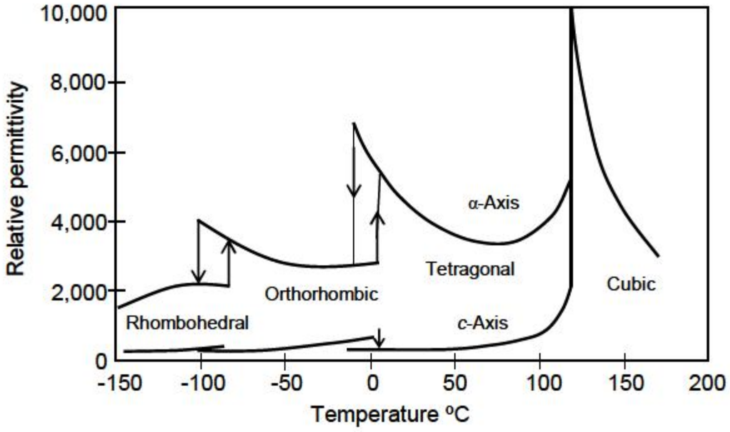

Fig. 1.2 Changes in dielectric constant in $BaTiO_3$ as a function of temperature and crystallographic form [Merz 1949 cited in Richerson, 2006]

The cubic form of BTO is stable only above its Curie temperature of about 135 °C [Swartz, 1990]. When an electric field is applied above its Curie point, the titanium ions shift from random to aligned positions, resulting in some bulk polarization but they return to their stable central position as soon as the field is removed. In this condition, the crystal is referred to as paraelectric [Richerson, 2006]. BTO has more than one ferroelectric phase. With cooling from its paraelectric cubic state [Swartz, 1990], It can exhibit with either ferroelectric tetragonal, orthorhombic or rhombohedral structures with transition temperatures of about 120 ºC, -10 °C and -100 °C respectively [Bailey, 2003]. As shown in Fig. 1.2, with an external electric field is applied, the titanate ions within the oxygen octahedral will move to the off-center position along the *c* axis resulting in a permanent diple [Richerson, 2006] below 120 °C. This is known as the cubic-tetragonal transition. Application of an electric field of opposite polarity to the original dipole will cause the Ti^{4+} ion to move through the centre of the octahedral site to an equivalent off-centre position on the other side [Richerson, 2006].

Further cooling results in conversion to an orthorhombic phase and then to a rhombohedra phase at approximately -10 ºC and -100 ºC respectively. The dielectric properties of BTO are not only dependent on the ferroelectric transitions between the various non-cubic phases but are also sensitive to grain size [Swartz, 1990]. For BTO with large grains, multiple domains will be found in a single grain. The walls motion of these domains provides a great contribution to the dielectric permittivity, especially at the transition temperature. However, for a fine-grained BTO, each grain can be regarded as a single domain. Thus, the dielectric constant at transition temperature will be lower because this domain will be clamped by the grain boundaries, which are not able to move freely. Hence, optimized properties can be achieved by appropriate control of the microstructure. The high dielectric constant of

BTO makes this material attractive for dielectric applications but its behavior is temperature and microstructure dependent [Swartz, 1990].

1.1.3 Ferroelectricity

Ferroelectric materials own permanent electric dipoles and therefore present a spontaneous polarization, which show polarization even without an external applied electric field. Among the 32 crystal classes, there are 21 crystal classes lack a center of symmetry. These classes may have several polar axes, which make them possible to show piezoelectric effects. Ferroelectric materials are one branch of pyroelectric materials. When an external electric field is applied on the ferroelectric crystal, it can reverse the spontaneous polarization of the sample. Thus, only from crystalline characterization' view, one cannot be sure with the ferroelectric materials. For the phenomenon of reversing spontaneous polarization, the experiment result will show it as a hysteresis loop. The shape of this hysteresis loop is quite similar with that of ferromagnetic materials [Haertling, 1999; Moulson, 1997].

1.2 Barium strontium titanate

Barium strontium titanate ($Ba_{1-x}Sr_xTiO_3$, abbreviated as BST) is a continuous solid solution of BTO and STO over the entire range of concentration x. According to the schematic drawing shown in Fig. 1.1, BST has perovskite (ABO_3) structure and can be considered to be occupied by Ba^{2+} and Sr^{2+} in the A-sites of the barium titanate lattice. [H. Landolt, 1981]. The high dielectric constant of BST may be caused by the ionic displacement. BST system only experiences an electronic displacement with the changing applied electric field. It can be seen from Fig. 1.1 that the Ti ions are surrounded by six oxygen atoms.

1.2.1 Structure-property relationship in (Ba, Sr)TiO_3

The structure-property relationship in BST has been well established in the literature [H. Landolt, 1981; Y. Gim, 2000; B. A. Baumert, 1998]. Both BTO and STO are typical ferroelectric materials, but at room temperature STO is in the paraelectric state. The transition temperature for ferroelectric state to paraelectric state of BTO is around 125 °C, while the transition temperature for ferroelectric state to paraelectric state of STO is around -233 °C. In BST system, the structure, dielectric and ferroelectric properties mainly depend on the Ba to Sr ratio. According to Fig. 1.4, the function of Curie temperature based on Ba/Sr ratio in bulk BST is exhibited. As the Ba content increases, the Curie temperature of BST increases linearly. This means, the tetragonality of BST system increases with increasing Ba content. The Ba rich phases are ferroelectric and tetragonal at room temperature. It is reported that, at room temperature BST is ferroelectric when the Ba content is over 65%. At room temperature, the $Ba_{0.65}Sr_{0.35}TiO_3$ has the highest dielectric constant because its tetragonal to cubic transformation is occurred approaching room temperature.

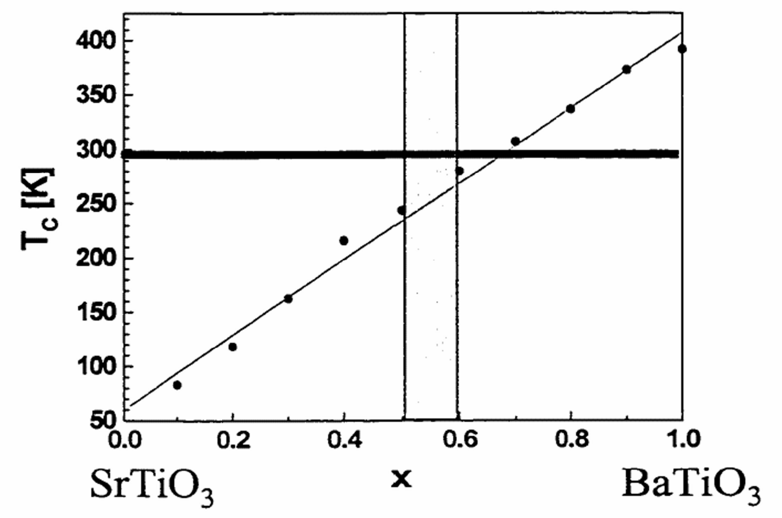

Fig. 1.4 Curie temperature of BST vs. composition [H. Landolt, 1981]

The lattice parameters (*a* and *c*) of BST system as a function of Sr amount at room temperature is given in Fig. 1.5. From Fig. 1.5, we can find that a tetragonal structure is shown on the high Ba content side, while cubic structure is shown on the high Sr content side. The cubic to tetragonal transformation boundary is around 0.3 of STO content, which is consistent with the dielectric test results. [H. Landolt, 1981]

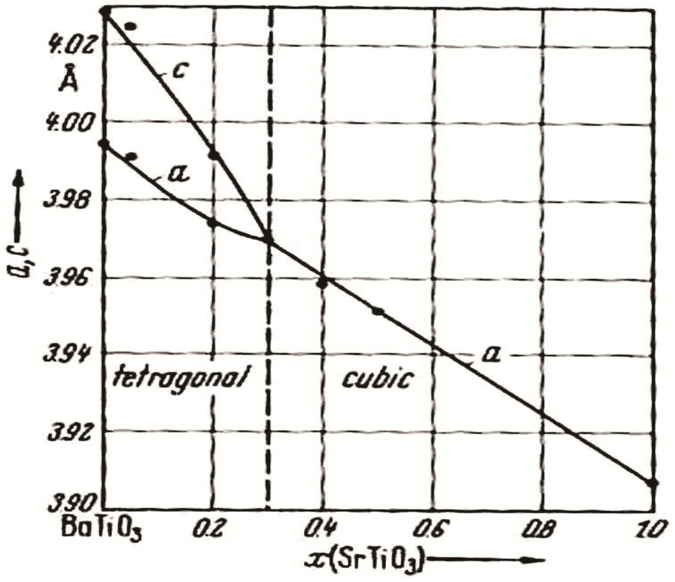

Fig. 1.5 Room temperature lattice parameter of BST versus composition [H. Landolt, 1981]

Fig. 1.6 shows a detailed temperature dependence of dielectric constant of BST with different compositions. In general, BST crystal has a relatively large dielectrc constant. According to Fig. 1.6, the maximum dielectric constant of $Ba_{0.6}Sr_{0.4}TiO_3$ is around 15000. The relatively large dielectric constant makes the BST ceramics to be one of the promising materials for the bulk capacitors fabrication.

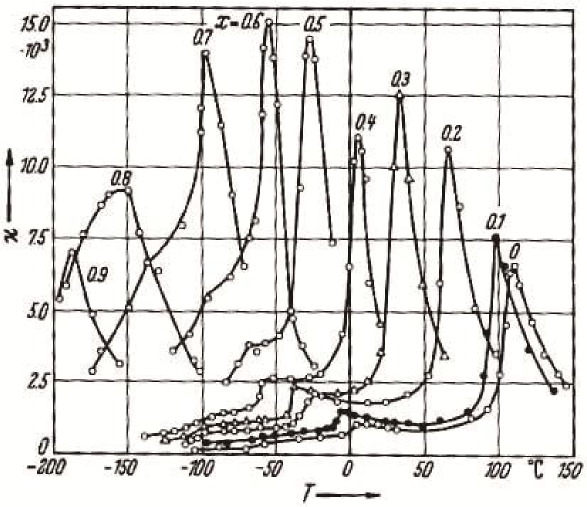

Fig. 1.6 Temperature dependence of dielectric constant of BST with different composition. [H. Landolt, 1981]

1.2.2 Study of (Ba, Sr)TiO_3 thin films

The main research interest in BST thin films are motivated by potential applications in integrated devices [D. Damjanovic, 1998], including infrared sensors [L. Dong, 2004] and thermal imagers [E. G. Kostsov, 1989], dynamic random access memory [C. L. Chen, 1999] and tunable microwave devices [M. W. Cole, 2002]. Different properties of BST are expected in these devices. For the tunable microwave applications, the BST thin film is required to exhibit a tunable dielectric property with small dissipation factor. Therefore it usually works in paraelectric phases. The advantages of BST thin films for applications in integrated devices include low operating voltages, smaller sizes and possible integration with semiconductor technology. Several literature results on the fabrication and structure-property relationship of BST thin film are summarized as below.

1.2.2.1 Deposition of (Ba, Sr)TiO_3 thin films

Many film growth techniques such as radio frequency magnetron sputtering, pulsed laser deposition (PLD), metallorganic chemical vapor deposition (CVD) and the sol gel process have been used to fabricate BST thin films [T. Y. Tseng, 1999]. Among these many methods available for the fabrication of thin films, the PLD method is the most popular method for basic research because it is easier to control the material composition and high quality thin films can be fabricated with a relatively high deposition rate.

1.2.2.2 Overview of structure and property relationship in (Ba, Sr)TiO$_3$ thin films

Similar to bulk BST materials, the structure-property relationship of BST thin films shows a significant dependence on the Ba/Sr ratio [Y. Gim, 2000]. Fig. 1.7 exhibits the function of lattice constant based on the Ba/Sr ratio for the BST thin film materials and BST ceramic materials. It can be found that both thin films and bulk materials show a very similar trend but the lattice constants of thin films are not the same as the ones of BST bulk materials with the same compositions. Fig. 1.8 shows a comparison of relationship in the phase transition temperatures versus Ba/Sr ratio for both BST thin films and bulk materials. The higher the ratio of Ba/Sr, the higher the transition temperature for BST systems will be. However, from Fig 1.8, we can conclude that for relatively small Sr contents, the transition temperature of BST ceramics are lower than that of BST thin film samples.

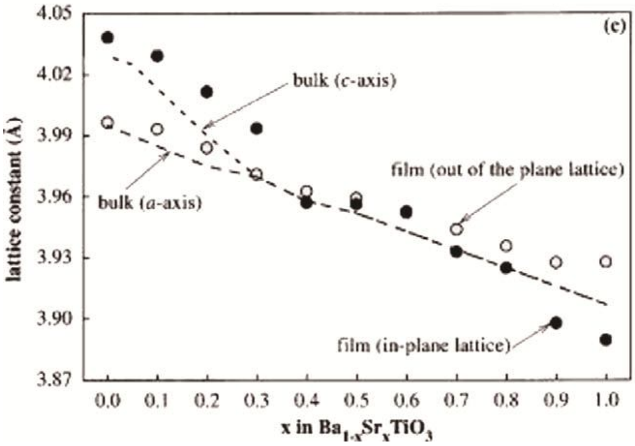

Fig. 1.7 A comparison of the lattice constant vs Ba/Sr ratio relationship in bulk and thin film of BST [H. Landolt, 1981; H. J. Gao, 1999].

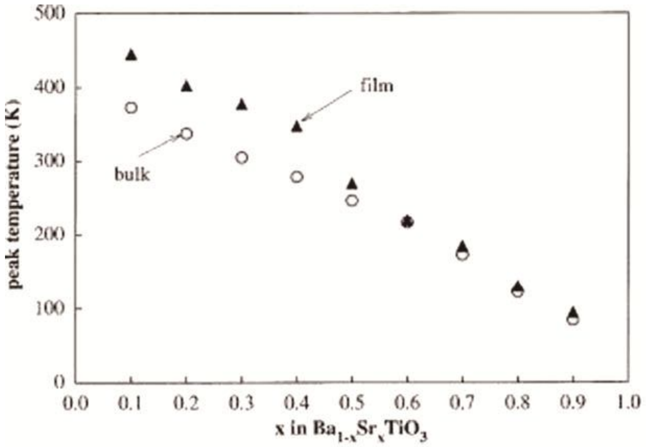

Fig. 1.8 A comparison of ferroelectric transition temperature vs Ba/Sr ratio relationship in bulk and thin film of BST [H. Landolt, 1981; H. J. Gao, 1999].

Film samples must need to be deposited on a substrate. The properties of the substrate will affect the structure and properties of the thin film samples. In BST thin films, the microstructure and phase transition is sensitive to lattice strain. Therefore, the main properties of BST thin film may be affected by the crystal structure, properties of the substrates. The measured capacitances of BST thin films on lanthanum aluminate (LAO) single crystal substrate is larger than that on magnesium oxide (MgO) single crystal substrate due to the different lattice strain. Therefore, investigations on the variations of structure and properties of thin films under stress by growing on different substrates will make sense to better understanding the phase transitions in related system.

1.2.3 (Ba, Sr)TiO_3 thin films for tunable microwave devices

1.2.3.1 Dielectric tunability and tunable microwave devices

When an electric field is applied to ferroelectric materials, the atomic structure of the materials might be changed and a nonlinear dielectric response can be exhibited. This property allows ferroelectric oxides to be one of the most interesting research topics for electronic applications. The dielectric constant is corresponding to the spontaneous polarization effect of ferroelectric materials. Loss factor determines the dissipative energy in the material. The commonly used figure of merit (FOM) for the quality of frequency and phase agile materials is a simple approach for relating the tunability and dielectric loss in a tunable material, the so-called *K* factor defined as :

$$K = \frac{\varepsilon(0) - \varepsilon(E_{\max})}{\varepsilon(0)} \frac{1}{(\tan\delta)_{\max}} \tag{1.3}$$

This *K* factor shows that tunable microwave devices can not take the whole advantage by a high tunability as well as a high loss factor. According to the previous literature, the reported K factor values are typically less than 50 [H. N. AL-Shareef, 1997].

In general, an ac signal is applied for a dielectric test. As shown in the figure, the DC electric field is applied upon the thin film sample. The relationship between dielectric constant and the external electric field is following the Johnson Equation [C. Zhou, 1997]:

$$\varepsilon(T,E)=\frac{\varepsilon(T,0)}{\left[1+(E/E_0(T))^2\right]^{1/3}} \tag{1.4}$$

where (T, E) and $\varepsilon(T, 0)$ are the dielectric constant under the electrical field E and zero field, respectively, and the $E_0(T)$ is a temperature dependent constant. From the equation, we can easily conclude that the maximum dielectric effect is happened with zero external electric field. With increasing the external field, the dielectric constant is decreasing. Fig. 1.9 exhibits a figure of relationship of dielectric constant on external DC electric field.

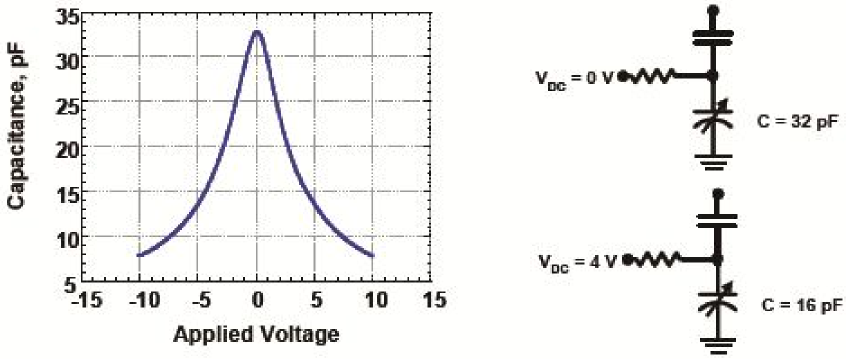

(a) (b)

Fig. 1.9 Schematic diagram show (a) Tunable dielectric behavior of ferroelectric material. (b) Capacitance of a ferroelectric oxide-based capacitor changes as external electric field changes.

The tunable characters of ferroelectric materials make it promising to be the materials for tunable microwave devices. The dielectric layers inside the capacitor devices can be produced by using ferroelectric materials. BST is a good candidate for such applications mainly due to:

(1)Dielectric and ferroelectric properties of BST can be easily modified by adjusting the Ba/Sr ratio;

(2)BST is relatively in the soft mode, especially when it works around the ferroelectric transition temperature.

1.2.3.2 (Ba, Sr)TiO_3 thin film-based microwave devices

As BST thin film materials have smaller size, lower operation voltage and it has possibility to integrate with semiconductor materials, it becomes very attractive for tunable devices applications [W. Chang, 1999; T. J. Zhang, 2007]. From the literature review, there already has a lot of research achievement for BST thin film-based microwave devices [H. Yoon, 2004; S. S. Gevorgian, 1996; R. Igrejil; K. B. Kim, 2007].

1.3 Integration of perovskite titanate with semiconductor

It has been a very attractive research topic for integration of perovskite titanate materials with semiconductor in recent years [M. Hong, 1999; R. A. Mckee, 2003]. At beginning, researchers try to improve the original MOSFETS to be a more complex metal/high-K/semiconductor system [G. D. Wilk, 2000]. The integration of perovskite oxide and semiconductor materials exhibit good electrical properties and quite lower defect in the structure because of the perovskite oxide thin films can be epitaxially grown on semiconductor surface. [C. J. Forst, 2004; R. A. Mckee, 2003].

Silicon is one of the most common used semiconductors for integration with other materials. Over the past decade, the $SrTiO_3$ (STO)/Si (001) epitaxial system has attracted intensive research interest, initially on purpose of identifying an alternative high-k dielectric for complementary metal oxide semiconductor (CMOS) technology. [R. Drooped, 2003; J. Ramdani, 2000]. Although it has been evidenced that STO was not appropriate for high-k application, efforts were continued to fabricate high-quality crystalline STO films on Si. In fact, fabricating high-quality STO/Si templates would open a new and monolithic path for the heterogeneous integration of new functionalities on the mature, low-cost silicon technology, since STO is the natural substrate for its isotype perovskite oxides, used in numerous functional devices such as ferroelectric field effect transistor (FeFET), nonvolatile memory and radio frequency filters, etc. [J.Heber, 2009; A.Ohtomo, 2004; P.Zubko, 2009; V.Garcia, 2009; J.F. Scott, 2007].

Compared with Si, GaAs has higher electron mobility and a higher saturated electron velocity. Besides, the devices fabricated based on GaAs semiconductor can work at much higher frequency with a very lower power supply. However, up to now, there are very few report about integration and properties characterization of perovskite titanate on GaAs.

1.4 Scope of the present study

Following the introduction given in this chapter, the thesis involves the following four chapters:

Chapter 2 gives a brief introduction to main techniques that have been used in the investigation, including pulsed laser deposition (PLD) and laser molecular beam epitaxy (LMBE) for thin film deposition, X-ray diffraction (XRD) for the characterization of crystal structure of thin films, atomic force microscopy (AFM) for determination of surface morphology, transmission electron microscopy (TEM), X-ray photoelectron spectroscopy (XPS) to study the interface of the heterostructure and dielectric property measurements.

In chapter 3, (Ba, Sr)TiO_3 thin films were deposited on GaAs substrates with a STO buffer layer by LMBE and their structure and surface morphology were investigated by using X-ray diffraction and atomic force microscopy, respectively. The interface structure and energy band of STO/GaAs was studied by TEM and XPS, respectively.

Chapter 4 describes electrode deposition on BST/STO/GaAs heterostructure. In-plane dielectric and ferroelectric properties of BST thin films were characterized by coplanar interdigital electrodes which have been patterned on the film surface.

Conclusions and suggestion for future work are given in Chapter 5.

1.5 Statement of original contribution

The main objective of our work on thin films is to conduct a systematic study on the dielectric and ferroelectric properties of BST thin films integration with GaAs substrate. To achieve that, LMBE technique was applied to obtain better quality BST thin films. Much emphasis was given to study the dielectric tunability and other related dielectric properties as function of temperature and the frequency.

The original contribution of the work presented in this thesis is summarized as follows:

1. $Ba_{0.7}Sr_{0.3}TiO_3$ thin films were fabricated on GaAs substrate with $SrTiO_3$ buffer layer by using O_2 flowing L-MBE technique.

2. Structure characterization of BST/STO/GaAs and STO/GaAs heterostructures were also performed by various techniques

3. Dielectric and ferroelectric properties of BST thin films on GaAs substrates under different conditions were analyzed.

CHAPTER 2

Techniques for deposition and structural characterization of perovskite titanate thin films

2.1 Introduction

The integration of perovskite titanate thin films with GaAs substrates is investigated by several advanced techniques and facilities for the deposition and characterization of the heterostructures. These techniques and facilities include:

(1) Techniques for thin film deposition: Pulsed Laser Deposition (PLD), Laser Molecular Beam Epitaxy (L-MBE).

(2) Electrode patterning: DC magnetron sputtering, spin coating, oxygen plasma and photolithography (for electrode patterning), wire bonding.

(3) Techniques for thin film structural characterization: X-ray diffraction (XRD), Scanning Electron Microscopy (SEM), Atomic Force Microscopy (AFM),

Transmission Electron Microscopy (TEM), X-ray photoelectron spectroscopy (XPS), Ultraviolet photoelectron spectroscopy (UPS).

(4) Electrical characterization: Dielectric properties measured by impedance analyzer: HP4294A was used for measuring frequency below 100 MHz, while HP4291B was used for the measuring frequency above 100 MHz. The ferroelectric properties were measured by the ferroelectric tester with model of TF Analyzer 2000.

This chapter will provide a brief introduction to these techniques which are particularly employed in our research work.

2.2 Deposition of perovskite titanate thin films

Perovskite titanate thin films have been grown by different techniques from the literature study, including physical vapor deposition method (PVD), such as radio frequency sputtering [T. Horikawa, 1993] and pulsed laser deposition (PLD) technique [L. A. Knauss, 1996], and soft chemical method, such as sol-gel [D. M. Tahan, 2005] and metalorganic vapor deposition (MOCVD) method [A. Tombak, 2002]. Among these thin film growing techniques, PLD is the most commonly used method.

In this thesis, the chemical composition of the thin film samples should be consistent with the perovskite titanate target. And the film should be epitaxial grown on the substrates. Among the grown techniques introduced above, PLD and L-MBE can control the composition and surface quality of the thin films. Thus, these two techniques were selected to be the major grown methods for this study. In general, these two techniques own similar growth mechanism and process control.

2.2.1 Pulsed laser deposition technique

The pulsed laser was applied as a direct energy source for thin film fabrication since the discovery of laser [Ramsey 1969; Smith and Turner 1969]. Early experiments were limited in scope, including continuous wave and pulsed lasers. The first experiment in pulsed laser deposition was conducted in 1960s. After that, several efforts were contributed to the technique in 1970s and 1980s. Then, in the late 1980s, the pulsed laser deposition was widespread as a fast and reproductive thin film growth method by its success of deposition *in situ* epitaxial high temperature superconducting films [England et al. 1988].

Pulsed laser deposition (PLD) is one of the thin film grown techniques with the physical vapor method. Many materials can be used by PLD. Several compound thin films are difficult to be fabricated by other techniques, can be produced by PLD technique. The PLD system consists three main parts: vacuum system, deposition chamber and laser system.

The principle of PLD is based on the interaction between laser and targets, carried out in a vacuum system. During the deposition process, a pulsed laser beam is focused onto the surface of the target with desired composition. For sufficiently high laser energy density, the material is ablated to create a plasma plume for every pulsed laser beam. The laser energy is transformed to electronic excitation and then into mechanical, chemical and thermal energy. This ablation process leads to ablation, evaporation, and plasma formation. There are several components in the plume, including atoms, molecules, electrons, and clusters and so on. The substrate should stand directly in front of the target surface. The target is evaporated and a plume with several components moves on to the substrate surface with highly orientation. The material forms the thin film on the substrate. PLD technique can be controlled with different conditions for thin film fabrication.

Fig. 2.1 Photograph of the PLD system used in this work.

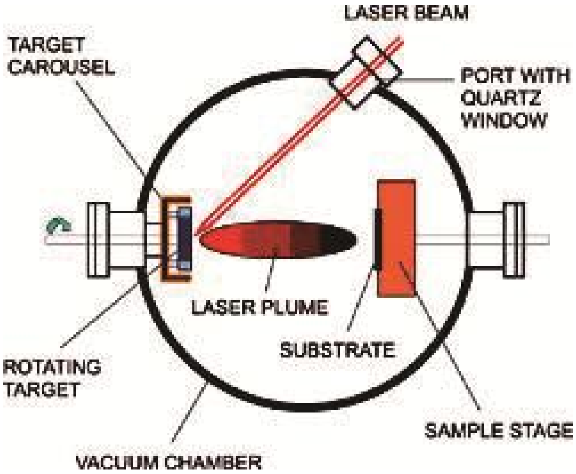

Fig. 2.2 Schematic illustration of the PLD chamber.

The photograph and schematic diagram of the PLD system used in this work are shown in Fig. 2.1 and Fig. 2.2, respectively. The PLD system consists of a KrF excimer laser with a wavelength of 248 nm and pulse duration of 25 ns (Lambda Physik COMPex 205); a rotating target holder with capacity to position various targets under the laser beam in order to fabricate multilayered heterostructure *in situ*; and a substrate holder which is designed that it can be heated to elevated temperature (T~750 ^{o}C) and can be rotated to ensure uniform deposition during the deposition process. The chamber vacuum is maintained by a turbo pump roughed with a rotary pump. In order to guide the laser light into the deposition chamber, an incident window should always be transparent to the incoming laser light. As the KrF excimer laser is used for fabrication, synthesized quartz is one of the preferred window materials. To avoid a reduction of laser energy onto the target, the window should be cleaned with special care before every fabrication.

The PLD method is widely used in the study of thin films. The advantages of this method include:

(a) Both single element and multi-component compound materials can be fabricated by PLD technique.

(b) The deposition rate is higher than other physical deposition techniques.

(c) Materials with high melting points can also be deposited if the materials absorb the laser light.

(d) The target composition is transferred to the film, leading to stoichiometric deposition.

The (d) point can be explained by the fact that, during the deposition process, the heating rate of the target surface is so high that it can lead to the congruent evaporation of the target irrespective of the evaporation point of the constituent elements or compounds of the target. Therefore, the stoichiometry of the target can be maintained in the deposited films. This feature is very useful when the composition of the material under investigation is very complex.

Several weak points for PLD also exist, including particulates splashing onto the films. For a relatively large area, the uniformity of the film is not very good for applications. Thus, PLD technique is not quite suitable for large area thin film applications. Therefore, the PLD has not been fully applied in industry. Simultaneous rotation of the target and substrate can help to improve the uniformity.

2.2.2 Laser molecular beam epitaxy

The principle of Laser molecular beam epitaxy (L-MBE) is quite similar from PLD. An introduction to PLD has provided in the above section. As all known, Molecular beam epitaxy (MBE) is one of the important thin film production equipment for both application and basic research. This technique is always used to produce semiconductor films. The advantages of MBE technique include clean growth environment, precise control of the growth condition, and easily implementation of *in situ* diagnostic instruments. The advantages of PLD and MBE can be combined to design a new technology. In 1983, J. H. Cheung *et al.* changed the traditional MBE equipment by replacing the molecular flux source by the solid target. [J. H. Cheung, 1983]. In 1991, M. Kanai *et al.* developed the MBE system with laser system for thin film growth [M. Kanai, 1991]. At this time, L-MBE becomes a new powerful tool for fabricating thin films. Comparing to PLD, L-MBE can provide ultra-high vacuum (UHV) environment and owns a structural characterization tool called reflection high energy electron diffraction (RHEED). RHEED is a technique for investigating the deposition mode during the thin film growth and characterize the surface structure. Comparing with PLD which grows thin film by an island growth mode, L-MBE with a RHEED system can grow the thin films with a layer-by layer mode

RHEED has a relatively high sensitivity for surface structure measurement which makes it to be one of the most important surfaces studying equipment in laboratory. There are several parts to constitute a RHEED system, including an electron gun, an observation screen and the software and hardware for the result treatment. A high energy electron beam, whose energy around 3 to 100 keV, can be produced by the electron gun. The beam is setting to hit the thin film surface with a relatively small angle. The electrons are diffracted by the crystal structure of the sample. The diffracted electrons hit onto the observation screen. The interference pattern can be found from the screen by the diffraction of the electrons. The interference depends on the crystal structure of the sample, so the pattern recorded contains information of the sample surface. On the other hand, a high vacuum growth environment is created by the pump system of LMBE. By this reason, it is possible to observe and control the quality of the surface of the thin film during the process of sample growth.

2.3 Structural Characterization

2.3.1 X-ray diffraction

X-ray diffraction (XRD) is a versatile, non-destructive technique to obtain the crystalline structure of single crystals, ceramics and thin films. In this project, XRD was employed to characterize the crystalline structure of the thin films produced. The lattice parameters of the thin films can also be determined by results of XRD.

2.3.1.1 Basic principle of XRD

The basic principle of crystal lattice measurement of samples by XRD is based on diffraction of X-ray waves which has the same order of wavelength with the lattice parameters in the crystal. Fig. 2.3 shows the basic geometry of XRD. From

Fig. 2.3, we can find the X-ray beam hit on the surface of the sample with an angle θ. Then the X-ray beam is diffracted by the surface with an angle θ. As all known, the constructive interference follows the Bragg's law, which describes as the transverse path difference between the two X-rays is the same as the integral number n times wavelengths of the X-rays. The Bragg's law can be expressed as the formula:

$$n\lambda = 2d_{hkl}\sin\theta \tag{2.1}$$

where d_{hkl} represents the distance between the parallel *(hkl)* lattice planes; λ represents the wavelength of the corresponding X-ray beam.

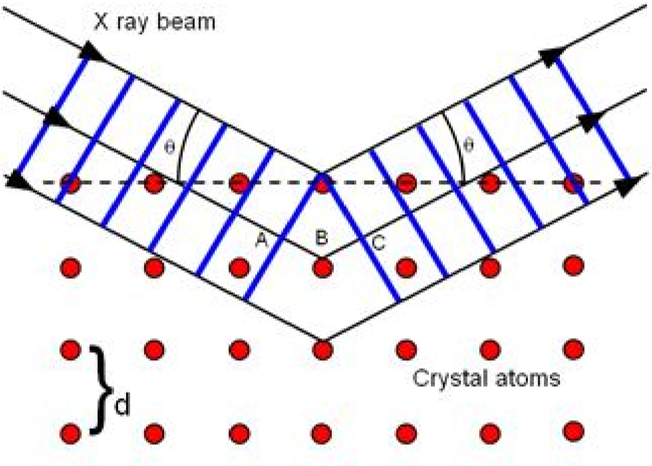

Fig. 2.3 Principle of X-ray diffraction for crystal structure characterization

2.3.1.2 X-ray diffractometer

The XRD measurement was perfomed on a Rigaku Smartlab high resolution X-ray diffractometer (HRXRD) with 9 kW rotating anode X-ray generators. This X-ray diffractometer includes a ceramic X-ray tube which has a Cu anode. The wavelength of Cu $K\alpha_1$ radiation is 0.15406 nm. There is a counter detector in the diffracted beam side, and several attenuators can be used in detector arm when it is needed. Sample is placed on sample holder on goniometer which allows for high-resolution θ-2θ measurement. The system also allows the rocking curves measurement in the sample-detector decoupled mode. Basically, a full characterization of structure of thin films needs a series of measurements, such as θ-2θ scan, rocking curve, φ-scan and ψ-scan as so on.

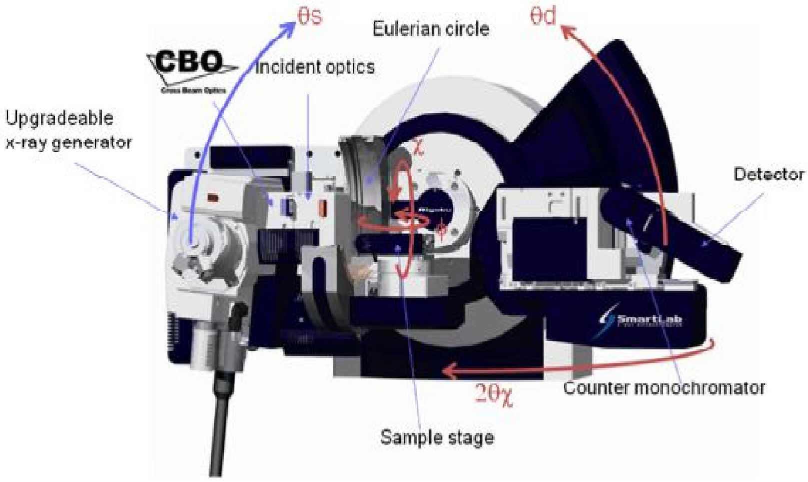

Fig. 2.4 Layout of the X-ray diffractometer

2.3.2 Atomic force microscopy

Scanning probe microscopy (SPM) has a number of different modalities such as scanning tunneling microscopy (STM), atomic force microscope (AFM), magnetic force microscopy (MFM), lateral force microscopy (LFM), etc. The first AFM was developed in 1986 by Binnig and his colleagues. In early 1990, the AFM techniques began to be used in the commercial field [Morris, 1999]. It is a non-destructive technique used for characterize the surface topography of the thin films, polymer coatings, and single-crystal substrates.

Fig. 2.5 shows the experimental setup of AFM. The AFM instrument consists of a cantilever, usually made of silicon nitride, silicon, or silicon oxide with a sharp tip mounted on its end. The tip is usually made from silicon nitride. Laser light is focused on the cantilever top and reflected to a segmented, position sensitive photo detector. The cantilever is brought close to the sample surface and raster scanned in the *x-y* direction using piezoelectric scanners. By keeping the photo detector signal constant and by varying the sample height through a feedback arrangement, it gives the vertical sample height variation compared to a base line. The principle of AFM is to measure the atomic forces between the experiment samples and the probes of the AFM. These forces depend on a number of factors such as the type of sample and probe, distance between probe and sample, and sample surface contamination. AFM does not require conducting samples and thus can be used for insulators, such as ferroelectric thin films.

AFM can operate in various modes. In contact mode the tip is in contact with the sample surface. In tapping mode, the tip is excited with vertical oscillations close to its resonance frequency. With the tip approaching the surface of samples, the attractive forces increase causing a decrease in resonance frequency. The distance between the tip and sample keeps constant during the measurement. In this mode the probe exerts negligible frictional force on the sample and therefore the surface damage is minimized. Our measurement was carried out in the tapping mode to determine surface microstructure, roughness of the (Ba, Sr) TiO_3 thin films on GaAs substrates with STO buffer layer.

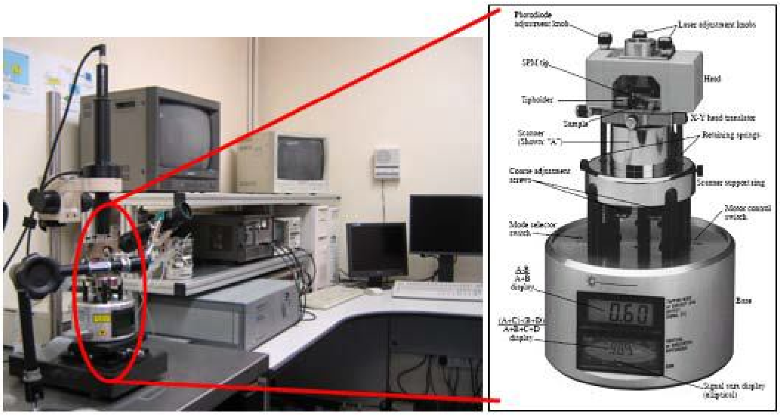

Fig. 2.5 Experimental setup of AFM.

2.3.3 Transmission Electron Microscopy

Transmission electron microscopy (TEM) is an important technique for materials characterization. The main principle of TEM is almost same as the common optical microscopy. TEM applies electrons as the measurement sources. There are several electromagnetic lenses included in the TEM system for focusing the electron beam. Before a typical TEM experiment, the samples should be pre-treated that their thickness is required to be kept around 50 nm. This relatively thin thickness allows the electrons easier to pass through the experiment samples. Several reactions will happen when the electron beam impinges on the sample surface. The beam will be diffracted by the surface. The diffracted beam will be focused by the objective lens, which makes an interference pattern on the back focal plane. There are several main TEM techniques for producing image and diffractions. They are including: selected are electron diffraction techniques; dark-field and bright-field TEM; Z-contrast imaging; high resolution TEM (HRTEM). For our research, JEOL JEM-2001 TEM equipment is applied. It can be worked at 200 kV. This equipment owns high-resolution, EDX and some other useful functions. Fig. 2.6 shows the picture of this type TEM.

Fig. 2.6 JEOL JEM-2001 TEM

2.3.4 X-ray photoelectron spectroscopy

When a sample surface is irradiated with photons of energy *hv*, electrons are emitted from the sample surface. This is called photoemission process. This process was first reported by H. Hertz in 1887 [H. Hertz, 1887]. The excitation source was a UV lamp. Nowadays, the excitation source can be X-ray or synchrotron radiation [C.

Nordling, 1957]. Here, we concentrate on the X-ray photoelectron spectroscopy (XPS).

The XPS can only analyze the top surface of the sample. The thickness of the layer that you can analyze is called the information depth. It depends on the ‘escape depth’ of the generated photoelectrons. A Restricted free path can also be found from the photons in the sample. However, this value is much higher than that of the electrons, thus it doesn’t restrict the information depth.

The instrument uses different pump systems to reach the goal of an UHV environment. The UHV environment will prevent contamination of the surface and aid an accurate analysis of the sample. Fig. 2.7 shows a picture of XPS system. When XPS works, a monoenergetic x-ray beam emits photoelectrons from the x-ray gun to the surface of the sample. Only about the top 10 -100 Å of the sample can be detected from the XPS spectrum. The binding energies can be determined from the peak positions and the elements present in the sample identified

Fig. 2.7 Schematic for XPS instrument

2.3.5 Ultraviolet photoelectron spectroscopy

The basic measurement principle of ultraviolet photoelectron spectroscopy (UPS) is similar to XPS but using a vacuum UV (10 - 45 eV) radiation to examine valence levels. In UPS, the radiation source is usually using a noble gas discharge lamp. For example, a He-discharge lamp emits He I radiation of energy 21.2 eV or He II radiation of energy 40 eV. UPS can ionize electrons from the outermost levels of atoms. Therefore it is usually applied to examine the valence levels of the samples while XPS is applied to examine the core-levels.

2.4 Dielectric and ferroelectric measurement

The dielectric properties measurements are conducted on an HP 4294 A (Hewlett Packard) impedance analyzer, which is applicable to measure and analyze the effective impedance of devices and circuits. Fig. 2.8 shows the picture of HP 4294A used in this work. The HP 4294A impedance analyzer can be used in a quite broad frequency range of 40 Hz - 100 MHz. The basic impedance precision of this instrument is ± 0.08%. Its exceptional high Q value precision makes it suitable for analyzing the low loss devices. The broad signal range can be used to evaluate the circuits in the practice working environment.

The measured signal level range is 5 mV to 1 V*rms* or 200 μA to 20 mArms. Advanced calibration system and error compensation function prevent the inaccuracy of measurement for devices measurement with clamping. Agilent 4294 A is a powerful tool for electronic components design, validation, mass control and fabrication tests. Electronic circuits design and development can also achieve the benefit from the functions and performance it provides.

A temperature controller ITC 601 (Cambridge, UK) was employed in the measurements to control the measurement temperature. Many devices' performance and properties may be affected by the temperature of environment. To keep the characteristics of devices unchanged in a changing environment, a temperature controller is required. The temperature controller can make the temperature sensor to be the input of the system. This controller is the main part of the temperature control system, which allows to accurately controlling the temperature during the measurement process. The controller compares the real temperature with the promising control temperature, and then export an output signal to the element controlled.

ITC 601 is a proportional-integral-derivative (PID) temperature controller, which is widely used in control systems of industry. Proportional values, integral values and derivative values are three main parameters for a PID controller system. The controller can satisfy the control requirements by tuning the three parameters. Some applications may not need all the three adjustments to offer the system control. One can set one or two parameters to be zero for these applications.

Fig. 2.8 HP 4294 A (Hewlett Packard) impedance analyzer.

In this work, the ferroelectric properties of the samples are measured by the ferroelectric analyzer with the model number of TF-2000, AixACCT Systems GmbH, and Germany. This equipment has a module which allows it works in the high-voltage state. The TF Analyzer 2000 is the most advanced analyzer for electro-ceramic materials and devices. Fig. 2.9 shows the main setup of TF 2000 used in this work. The ferroelectric standard testing is based on the FE module, which can be used in different performance levels. For the ferroelectric analyzer, it can measure for the frequency between 1 mHz to 5 kHz. The primary electronic properties of the ferroelectric samples can be measured by the TF analyzer 2000 FE which is the ferroelectric test module. For the FE module, it can be applied to measure the hysteresis loop, fatigue properties, retention properties and leakage current. Moreover, FE module can also be used to do the piezo measurement, pyroelectric measurement and impedance measurement.

Fig. 2.9 TF 2000 ferroelectric analyzer

2.5 Summary

Several advanced techniques are applied in the fabrication and characterization of BST thin films. In this chapter, we have only introduced five typical techniques. Thin film samples can be prepared by PLD. The structure of the thin films can be characterized by XRD, AFM, TEM, XPS and UPS. Several dielectric and ferroelectric measurement instruments are also introduced. And In the following chapters, more discussions on the fabrication and characterization techniques may be given whenever necessary.

CHAPTER 3

Growth and structural characterization of perovskite titanate thin films

3.1 Introduction

Perovskite titanates are very attractive materials which can be used for a variety of devices [I. Vrejoiu, 2008; T. Yajima, 2011; J. H. Hao, 1996]. Among these devices, frequency and phase agile microwave devices have widespread applications. For electric-field tuning, the ferroelectrics of choice are mostly (Ba, Sr)TiO_3, where the Curie temperature depends on the Ba/Sr ratio, and can be adjusted from 40 K for $SrTiO_3$ (STO) to 398 K for pure $BaTiO_3$ [X. X. Xi, 2000; C. L. Chen, 2001]. The high dielectric constant, low dielectric loss, and the dielectric nonlinearity are the materials parameters that enable such applications. However, the problems are the high cost of the substrates and the fact that oxide substrates of MgO and LAO are only available in small geometries which are not suitable for mass production [M. W. Cole, 2002]. Additionally, the use of oxide substrates requires mounting complicated hybrid microwave integrated circuits.

In order to solve these problems, BST films were integrated on a normal silicon (Si) substrate directly [H. -S. Kim, 2005]. As Si wafers are extensively used in industry and enable the large size fabrication, a mass production process of BST-based devices is available. However, the tunability of BST/STO heterostructure is low because of the SiO_2 thin layer between BST and Si. The SiO_2 layer is generated by the oxidization of Si substrate during the high-temperature BST deposition process [A. H. Meuller, 2002]. In addition, the dielectric loss is very high due to the low resistivity of Si [H. -S. Kim, 2005]. A heterostructure of BST layer deposited on high resistivity Si (HR-Si) with a TiO_2 buffer layer can solve these problems. Because the HR-Si serves as a barrier against the realization of BST and TiO_2 buffer layer controls the orientation and quality of the BST films [M. W. Cole, 2002]. Fig. 3.1 shows the normalized capacitance characteristics of the BST thin films grown on TiO_2/normal Si (10 Ωcm), TiO_2/HR-Si (2 kΩcm), and MgO substrates as a function of bias voltage from 0 V to 40V in microwave frequency of 2 GHz. According to the figure, BST films grown on TiO_2/normal Si show a tunability of 8.2% at an applied voltage of 40 V, which is much smaller than that of the dielectric measurement at 1 MHz for BST/TiO_2/normal Si structure revealed a tunability of 72.9% at 10V [I. D.

Kim, 2004]. The dielectric loss is very large for BST integrated with low resistivity Si at high frequency. While for the HR-Si, the tunability value of the BST film was much improved up to 33.2% at an applied voltage of 40 V. This value is also larger than that of BST thin films epitaxially grown on a MgO single crystal substrate (Tunability = 21%).

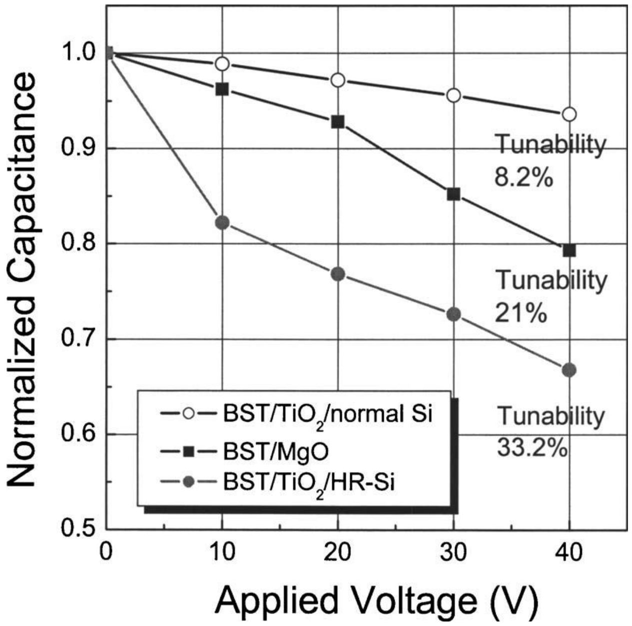

Fig. 3.1 Normalized capacitance-voltage characteristics of BST films grown on MgO, TiO_2/ normal Si, and TiO_2/HR-Si. [Hyun-Suk Kim, 2005]

Compared with Si, III-V semiconductor materials have some electronic properties which are superior. III-V semiconductor materials with flexible engineering of band-gap properties, have high electron mobility, and find many applications in photonic and electronic devices [M. Hong, 1999]. Gallium arsenide (GaAs) is a compound of the elements gallium and arsenic, which is one of the typical III-V semiconductors. Compared with Si, GaAs devices are relatively insensitive to heat due to their higher band gap. Also, GaAs devices tend to have less noise than silicon devices especially at high frequencies which are a result of higher carrier mobility and lower resistive device parasitic. Above properties indicate that GaAs will be a potential application for the transistors with a high speed but working with a low power supply [R. Chau, 2005]. Fig. 3.2 provides the relationship between electron velocity and the electric field for both pure GaAs and Si. Because of its wide band gap, pure GaAs has very high resistivity. Combined with the high dielectric constant material, this property makes GaAs a very good electrical substrate. Based on the above analyses, it is quite attractive for the integration of perovskite titanate thin films with GaAs substrates. This heterostructure could be a basis component for a lot of applications. For example, GaAs-based metal-ferroelectric-insulator-semiconductor (MFIS) functional heterostructures was invented [M. Hong, 1999; M. Passlack, 2002; K. D. Choquette, 1997]. Fig. 3.3 exhibits two in plane microwave devices with different structure.

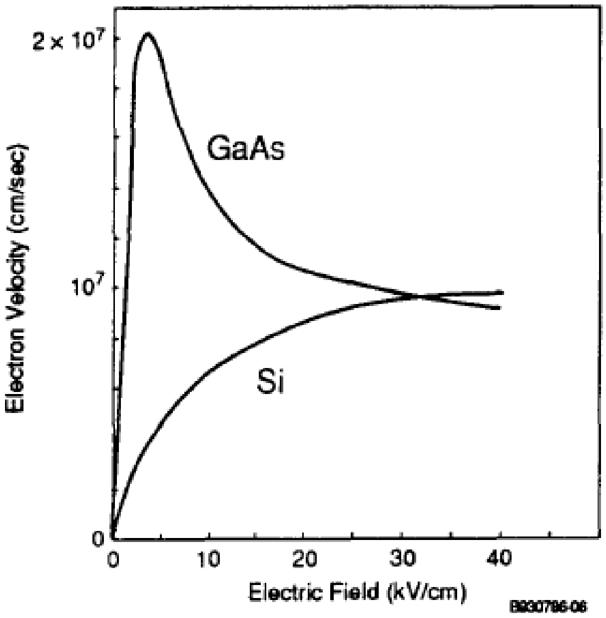

Fig. 3.2 Relationship between electron velocity and electric field for pure GaAs and Si [D. E. Fulkerson, 1992].

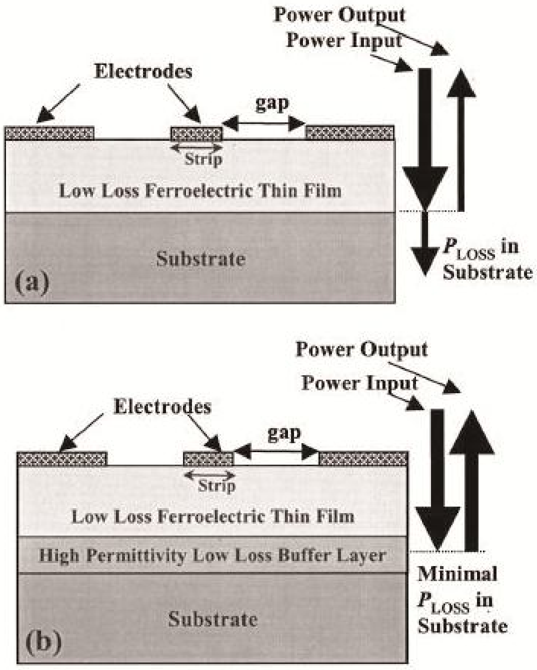

Fig. 3.3 Two different coplanar device designs [M. W. Cole, 2002].

In the last decades, the epitaxial perovskite titanate thin films on silicon substrates are quite attractive. [R. A. Mckee, 1998; H. Li, 2003; J. H. Hao, 2005; J. L. Li, 2007], while integration with GaAs has attracted much less attentions. From the literature study, epitaxial BTO thin films grown on GaAs substrates with a MgO buffer layer has been prepared successfully. The interface structure and the thickness of the MgO buffer layer could affect the ferroelectric properties of the heterostructure. [T. E. Murphy, 2004]. It suggests that the epitaxial buffer layer and the interface to property relationship become critical problems for GaAs-based ferroelectric devices. Based on the Breton's study, for the heterostructure of a very thin MgO film with around few nanometers deposited on the GaAs substrate, the current effect in the interface results in the increasing of reverse bias voltage. This effect will lead to high charge injection for the heterostructure [J. C. Le Breton, 2007]. Ferroelectric oxides deposited on GaAs with MgO buffer layer always show weak ferroelectricity with a large leakage current [T. E. Murphy, 2004].

Compared with MgO, $SrTiO_3$ (STO) owns a large dielectric constant and low dielectric loss. STO is a common incipient ferroelectric material. The single crystal form of STO has low interface defect and own good electrical properties, which makes it to be one of the promising materials for the electrical applications. So far, epitaxial STO thin films have been successfully grown on GaAs substrate by laser molecular beam epitaxy (LMBE) [Z. P. Wu, 2008]. The structure of STO is cubic perovskite. Its lattice parameter matched very well with many other functional oxides. Improved electrical properties of functional oxides grown on STO buffered GaAs are presented [W. Huang, 2009; W. Huang, 2010]. As the single-crystal oxide substrates have high cost and small geometries for applications in tunable microwave devices, they could be replaced by the commercial GaAs wafers with high-performance microwave capabilities and large-size availability. Hence, it is of great interest to explore the heterostructure consisting of BST and GaAs, aiming at room temperature tunable device.

Based on the literature review, we have conducted experiments on integration of BST thin films on GaAs substrates. The BST that we chose to investigate has a composition of $Ba_{0.7}Sr_{0.3}TiO_3$ since the Curie temperature of this composition is near room temperature and its room-temperature dielectric tunability is very large [Y. Lin, 2004]. In this chapter, the details of fabrication epitaxial BST thin films on GaAs substrate with a STO buffer layer by pulsed laser deposition technique will be provided. The crystalline structure was investigated by X-ray diffraction (XRD) technique. The surface morphology and interfacial structure of perovskite titanates/GaAs heterostructure were studied by atomic force microscopy (AFM) and transmission electron microscopy (TEM), respectively. The chemical valences of BST thin films on STO/GaAs and energy band at the interface of STO/GaAs were investigated using the photoelectron spectroscopy. The dielectric and ferroelectric characterization of the BST/STO/GaAs heterostructure will be presented in the next chapter.

3.2 Thin film deposition by laser molecular beam epitaxy

In this study, The BST thin films were deposited on high resistivity GaAs (001) substrate ($\rho > 1\times10^{6}\,\Omega$.m) with a STO buffer layer by pulsed laser deposition system with O_2 flowing. The laser system has an operation wavelength of KrF (λ = 248 nm). The distance between target and the substrate was about 5 cm. The STO buffer layer was first deposited on GaAs substrate as described in our previous report [Z. P. Wu, 2008]. The deposition temperature was set around 600 °C for STO thin film grown on GaAs. To prevent the GaAs substrate from oxidizing, the chamber was evacuated to a base pressure of 5×10^{-5} Pa during the STO thin film deposition. The deposition time was 10 min with 1Hz laser repetition rate, resulting in an approximately 10 nm thick STO layer. After that, the STO/GaAs was heated up to 620 °C and the oxygen partial pressure was fixed at 1 Pa for the subsequent BST layer deposition. The oxygen pressure used here is relatively small because the GaAs substrate could be oxidized by a larger oxygen pressure, which could decrease the crystallinity of the heterostructure. The thickness of the BST thin film was around 300 nm. In order to reduce the oxygen vacancies in the thin film, the heterostructure were then *in situ* annealed with 200 Pa oxygen pressure for 1 hour after the deposition process. Then the samples could be taken out from PLD chamber after being cooled down to room temperature. The conditions for BST thin films deposition are provided in table 3.1 and table 3.2.

Table 3.1 L-MBE deposition conditions for STO buffer layer on GaAs.

Target	STO single crystal
Laser energy	6 J/cm^2
Laser wavelength	248 nm
Deposition Frequency	1 Hz
Pre-annealing temperature	620 °C
Pre-annealing time	2 min
Target-substrate distance	50 mm
Base pressure	5×10^{-5} Pa
Growth pressure	1.6×10^{-4} Pa
Growth rate	0.02 nm/pulse
Substrate temperature	580 °C

Table 3.2 L-MBE deposition conditions for BST thin film on STO buffered GaAs.

Target	BST ceramic
Laser energy	6 J/cm^2
Frequency	1 Hz
Target distance	6 cm
Pressure	O_2: 1 Pa
Substrate temperature	600 °C
Annealing temperature	420 °C
Annealing time	1 hour

3.3 Crystallization Characterized by XRD

Fig. 3.4(a) shows a typical *θ-2θ* XRD for the BST thin films prepared by the above precedures. As observed from the figure, only (*00l*) peaks of the BST appear in the diffraction patterns besides the peaks from GaAs wafer. It suggests that the BST thin films have a single perovskite phase and are highly oriented along *c*-axis. Since the small thickness of STO layer, obvious peaks corresponding to STO can not be found in Fig. 3.4(a). Rocking curve measurements presents a full width at half maximum (FWHM) value of 1.1° in the inset of Fig. 3.4(a). This value is larger than that of the previously reported BST films on single-crystal substrates. For example, the FWHM value of BST thin films grown on MgO substrates and LAO substrates are around 0.54° and 0.15°, respectively [S. E. Moon, 2003; H. -J. Gao, 1999]. At room temperature, the lattice parameters for the bulk BST are $a = b = c = 3.965$ Å [D. Y. Wang, 2005]. Calculation based on Figure 3.4(a) results in c-axis lattice constants of 3.992 Å and 5.653 Å for BST thin film and GaAs substrate, respectively. It was observed that the lattice parameter of BST thin film is slightly larger than that of bulk BST, which suggests that the BST film suffered from a compressive strain caused by the lattice mismatch between BST and the underlying cubic STO buffer layer (a = 3.903 Å). In Figure 3.4(b), the off-axis Φ scans of the BST film and GaAs are provided. The (110) diffraction peak for the Φ scans measurement is picked up from the BST film. Only four peaks, 90° apart, are shown for the BST films, which are at the same angles with GaAs wafer. From the Φ scans results, we can conclude the BST film is epitaxially grown on the (001) surface of STO. The heterostructure has an in-plane film-substrate orientation relationship of [100]BST||[100]STO||[110]GaAs.

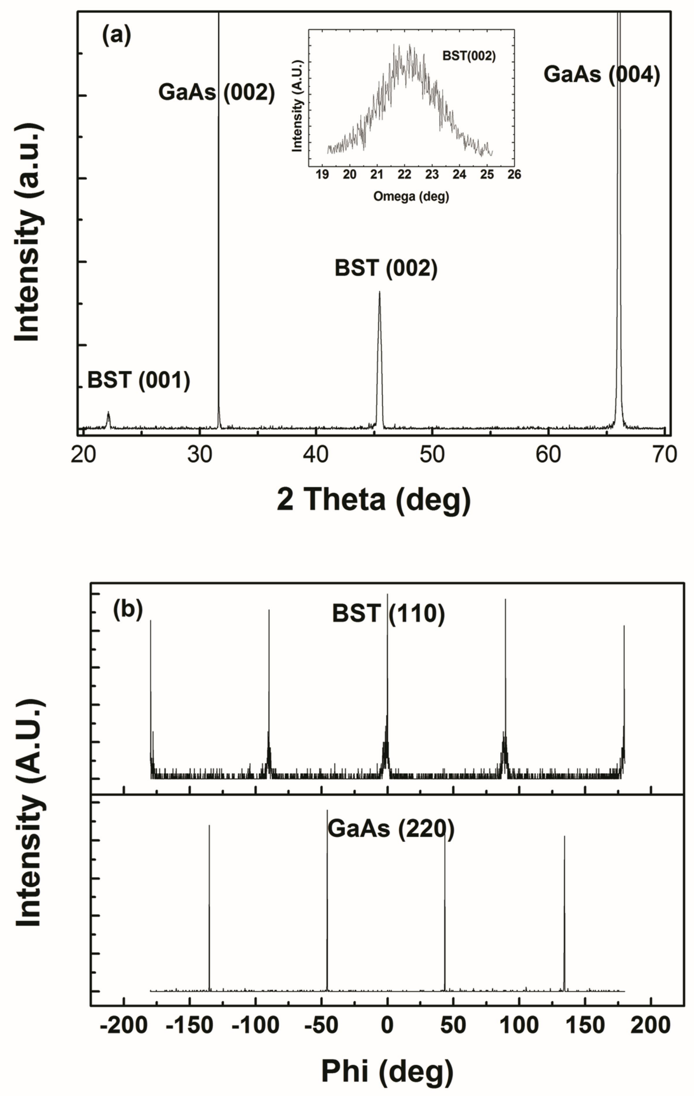

Fig. 3.4 XRD pattern of BST/STO/GaAs (001) heterostructure. (a) *θ-2θ* scan. The inset indicates the rocking curve for BST (002); (b) Phi scan of (110) reflections of the BST thin film and GaAs (220) substrate.

3.4 AFM Morphology of (Ba, Sr)TiO_3

Typical AFM images taken from the surface of the BST film in Fig. 3.5 confirm the high quality structure of the BST films. From the AFM measurement, we can conclude the as-grown film has very smooth surface. Its root-mean square (rms) roughness values is around 1.60 nm. Our results are superior to the rms roughness value measured from BST thin film grown on other substrates. For example, the rms values of BST thin films grown on MgO substrates and MgAlO substrates are 2 nm and 2.3 nm, respectively [D. Y. Wang, 2005; X. Y. Zhou, 2006]. Such good surface makes the thin films suitable for fabricating devices with in-plane electrodes.

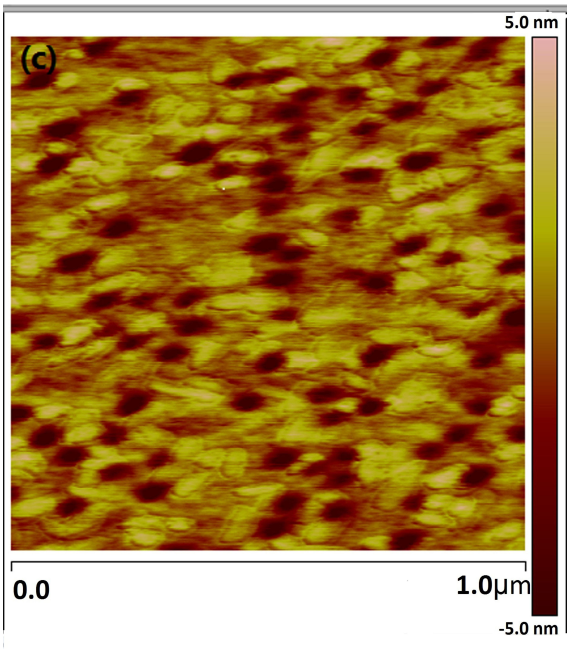

Fig. 3.5 AFM pictures of the surface of heterostructure of BST thin films (~300 nm) on GaAs substrate with STO buffer layer (~10 nm).

3.5 Interfacial Structure of perovskite titanates on GaAs

In order to investigate the interfacial structure of perovskite titanates on GaAs heterostructure, TEM technique was performed on STO/GaAs (001). Fig. 3.6 (a) gives the cross-sectional high-resolution TEM (HRTEM) image of the epitaxial STO thin films on GaAs substrate. The sharp interface transition suggests that the STO film has good crystallinity. The sharp STO/GaAs interface indicates the good alignment of the two lattices. The bright/dark contrasts at the interface result from the strain distribution around interfacial misfit dislocations [Y. Liang, 2004]. Fig. 3.6 (b) shows the corresponding selected area electron diffraction (SAED) pattern, which indicates a crystalline orientation relationship of (001) [100] STO|| (001) [110] GaAs. Such an orientation relationship is consistent with the small lattice mismatch between STO and GaAs going through a 45° in plane rotation [Z. P. Wu, 2008].

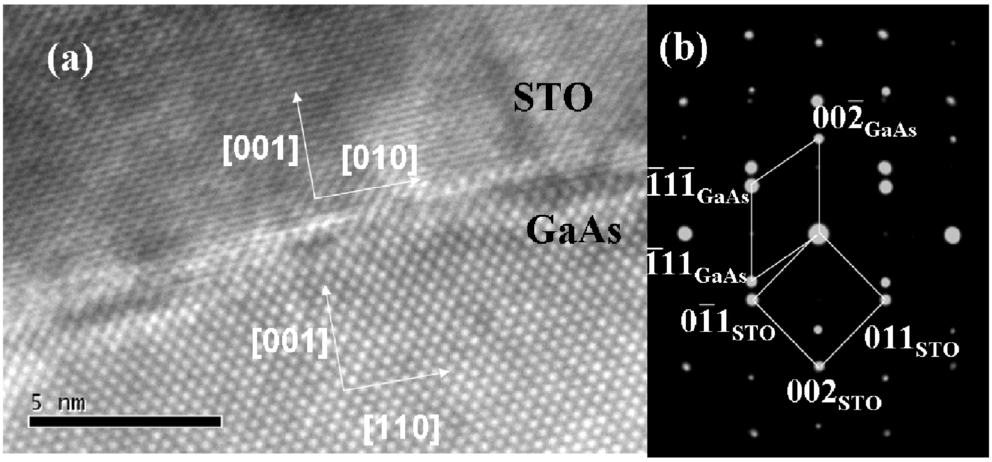

Fig. 3.6 (a) Cross-sectional HRTEM image of STO/GaAs; (b) SAED pattern at the interface of STO/GaAs.

3.6 Structural Characterization by XPS

3.6.1 XPS analyses for chemical structure of the BST films

X-ray photoelectron spectroscopy analyses were used to study the chemical bonding energies of the elements of the interface between $Ba_{0.7}Sr_{0.3}TiO_3$ thin film and STO buffer layer. A thick 2 nm BST thin film grown on STO (10 nm)/GaAs was studied. Fig. 3.7 shows the XPS survey spectrum of the BST thin film within the binding energy range of 0 eV to 1000 eV. As shown in the figure, the BST thin film contains five elements of Ba, Sr, Ti, O and C. The existence of carbon may be generated by the pumping oil. No other impurity element was found in the binding energy range of 0 - 1000 eV.

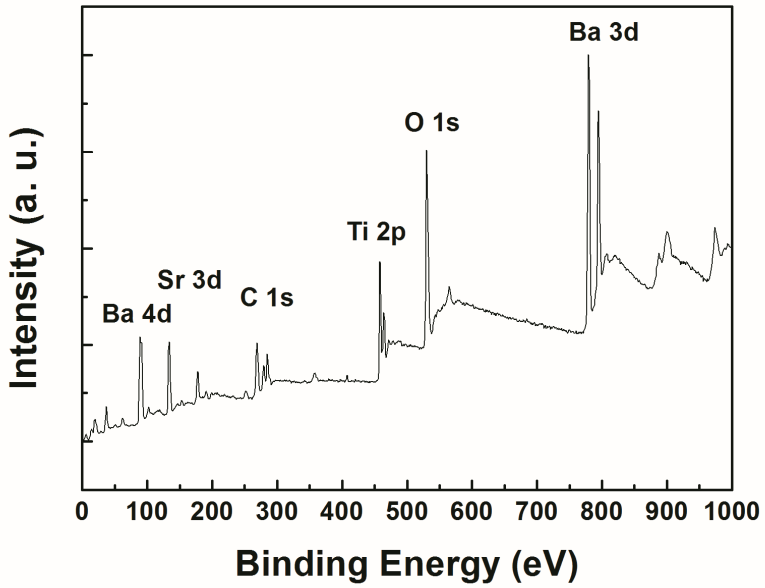

Fig. 3.7 The XPS spectrum of the $Ba_{0.7}Sr_{0.3}TiO_3$ thin films in the binding energy range of 0-1000 eV.

The XPS spectrum peaks of Ba, Sr, Ti, and O elements are provided in Figs. 3.8 (a) - (d) respectively. According to the Fig. 3.8 (a), the two binding energy peaks of Ba element are at 779.4 eV (Ba $3d_{5/2}$) and 794.7 eV (Ba $3d_{3/2}$). These two energy positions are similar to the standard values of Ba in BaO (779.65 eV and 795.0 eV) [C. D. Wagner, 1979]. Thus the state of chemical valence of Ba in $Ba_{0.7}Sr_{0.3}TiO_3$ thin films is fixed to be +2. From the Fig. 3.8 (b), the two binding energy peaks of Sr element are at 133.7 eV (Sr $3d_{5/2}$) and 135.4 eV (Sr $3d_{3/2}$), which are quite consistent with the earlier reported values for SrO spectrum (133.7 eV and 135.5 eV) [C. D. Wagner, 1979]. Fig. 3.8 (c) shows the XPS peaks for Ti *2p* of BST at 459.0 eV (Ti $2p_{3/2}$) and 464.8 eV (Ti $2p_{1/2}$) with a 5.8 eV doublet splitting, which is in agreement with the XPS characteristics of TiO_2 [D. J. Gao, 2003]. The O_{1s} peak is located at 530.2 eV presented by Fig. 3.8 (d). This value is similar with the previous reported XPS study values of strontium titanate films on titanium [M. E. Pilleux, 1994]. Thus, we can conclude that the valence states of Ba, Sr ,Ti and O elements of $Ba_{0.7}Sr_{0.3}TiO_3$ thin films grown on STO/GaAs are +2, +2, +4 and -2, respectively, which is consistent with the standard BST compound.

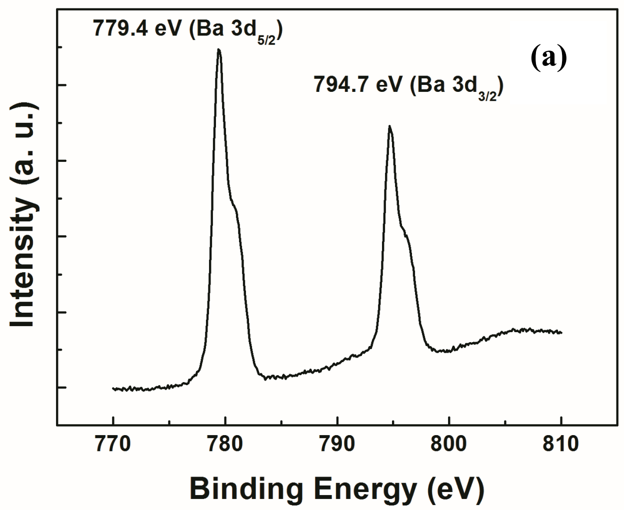
779.4 eV (Ba $3d_{5/2}$)
794.7 eV (Ba $3d_{3/2}$)
(a)
Intensity (a. u.)
770
780
790
800
810
Binding Energy (eV)

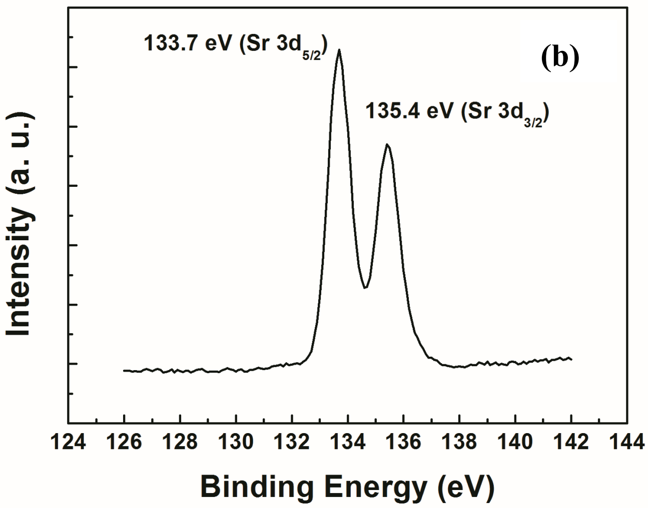
133.7 eV (Sr $3d_{5/2}$)
135.4 eV (Sr $3d_{3/2}$)
(b)
Intensity (a. u.)
124
126
128
130
132
134
136
138
140
142
144
Binding Energy (eV)

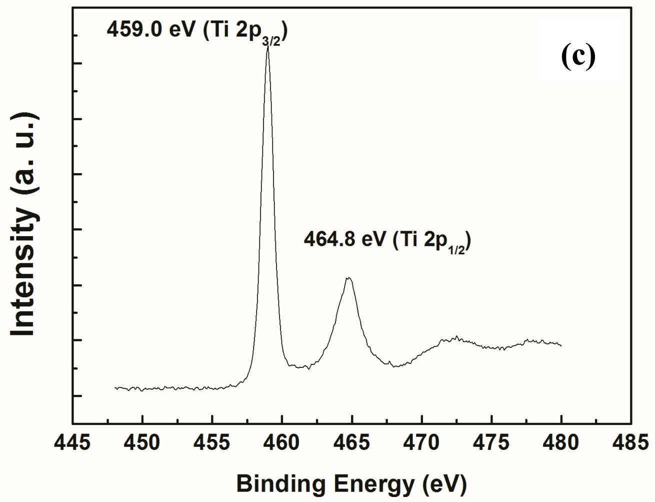

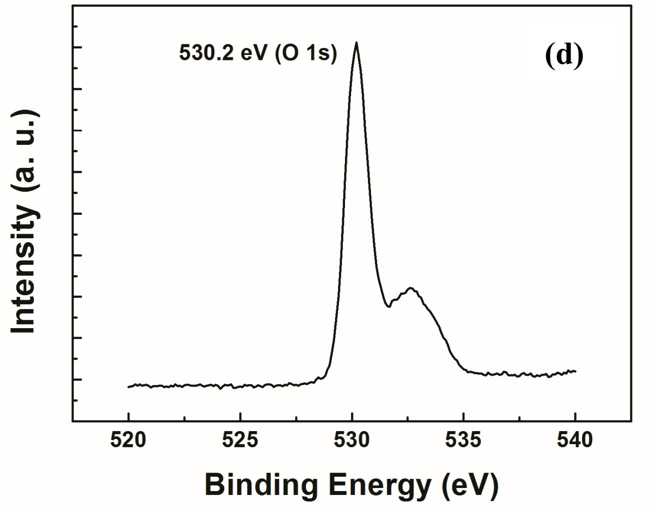

Fig. 3.8 XPS spectra for (a) Ba, (b) Sr, (c) Ti, (d) O of $Ba_{0.7}Sr_{0.3}TiO_3$ thin films respectively.

3.6.2 Energy band study of STO/GaAs

The energy band information is one of the significant issues for perovskite oxide/III-V interface since it can illustrate the mechanisms of actions occurs in the perovskite oxide/III-V based devices. For instance, the metal-oxide-semiconductor field-effect transistor (MOSFET) involving functional oxide/GaAs heterostructure need sufficient band offsets to be reached and the Fermi level should be unpinned at the oxide/GaAs interface [Y. Liang, 2005]. During the past 40 years, it had attracted considerable interest to find an appropriate oxide which can provide adequate interface to combine with GaAs [C. W. Wilmsen, 1985]. Some amorphous or poly-crystalline films, such as Ga_2O_3 and Ga_2O films were reported to be unpinned the Fermi level [M. Passlack, 1996; M. Hale, 2003]. Compared with them, integration of single crystal perovskite oxides with GaAs may be superior because of better interface structure and ease of structure and property relationship in an epitaxial system [Y. Liang, 2005].

In this thesis, we present photoemission studies on energy band at the interface of STO thin films on high resistivity GaAs substrates. The heterostructure was fabricated by L-MBE. The details on the film deposition procedures are provided in the previous chapter. As a great deal of electrons is excited to emit from the thin film, the film always appears as positive charge. The electric field caused by the positive charge may affect the kinetic energy of photoelectrons for XPS study. Therefore, the binding energies at various peaks were all calibrated by the C *1s* peak (284.6 eV) [D. J. Gao, 2003]. The calibration for the absolute value of binding energy does not affect the final result， because the valence band offset (VBO) values are only determined by the relative position of the samples. Thus, only relative energy differences are considered in this work. The valence band offset (VBO) $\triangle E_v$ can be calculated from the formula:

$$\Delta E_v = (E_{cl}^{GaAs} - E_v^{GaAs})^s - (E_{cl}^{STO} - E_v^{STO})^f + (E_{cl}^{STO} - E_{cl}^{GaAs})^{\mathrm{int}} \qquad (3.1)$$

where $(E_{cl}^{GaAs} - E_v^{GaAs})^s$ and $(E_{cl}^{STO} - E_v^{STO})^f$ are the difference of the core levels (CLs) and the valence band maximums (VBMs) of clean high-resistivity GaAs substrate and 150 nm thick STO film, and $(E_{cl}^{STO} - E_{cl}^{GaAs})^{\mathrm{int}}$ is the difference of CLs between the 2 nm thick STO thin film and GaAs substrate, respectively. In general, there are two steps to determine the VBO of the heterostructure. First, we determine the energy difference between the VBMs and CLs for both GaAs substrate and thick STO film. VBMs and CLs were measured by UPS and XPS technique, respectively. Second, we determine the energy difference of CLs between STO film and GaAs substrate of STO/GaAs heterostructure.

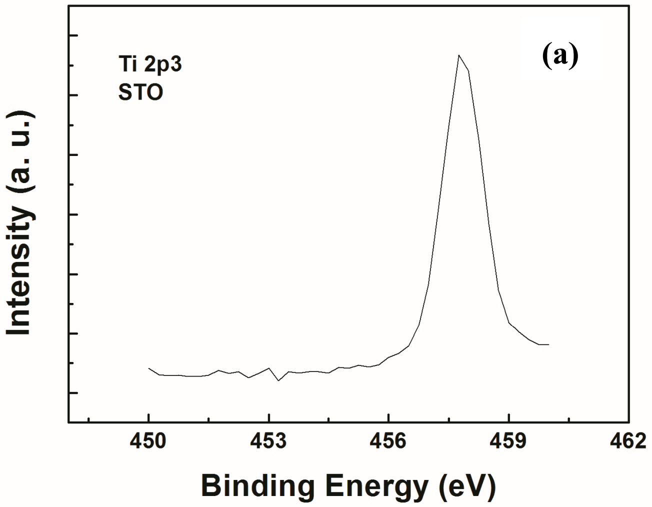

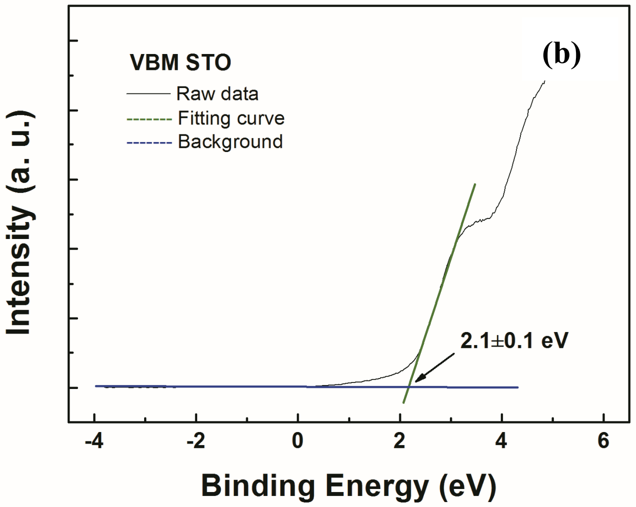
VBM STO
(b)
Raw data
Fitting curve
Background
2.1±0.1 eV
Intensity (a. u.)
Binding Energy (eV)
-4
-2
0
2
4
6

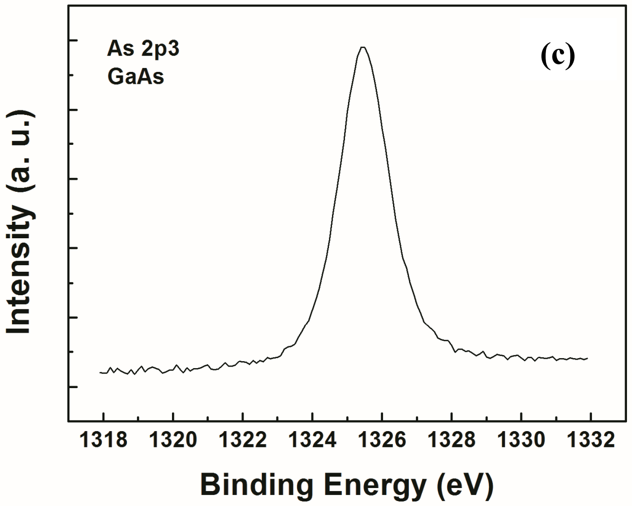
As 2p3
GaAs
(c)
Intensity (a. u.)
Binding Energy (eV)
1318
1320
1322
1324
1326
1328
1330
1332

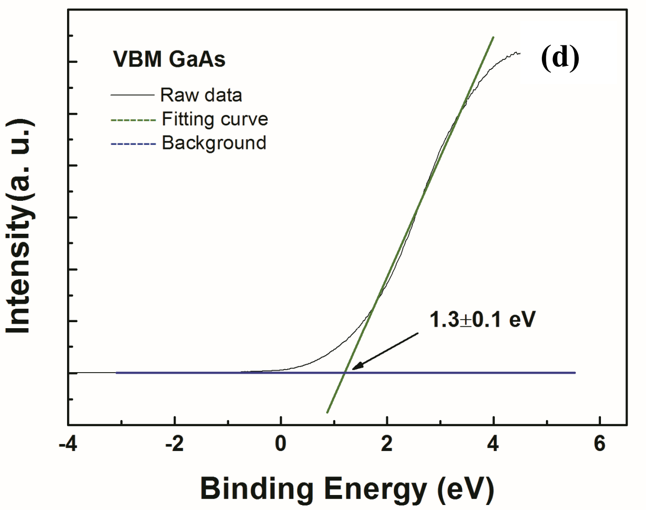
VBM GaAs
Raw data
Fitting curve
Background
(d)
1.3±0.1 eV
Intensity(a. u.)
Binding Energy (eV)
-4
-2
0
2
4
6

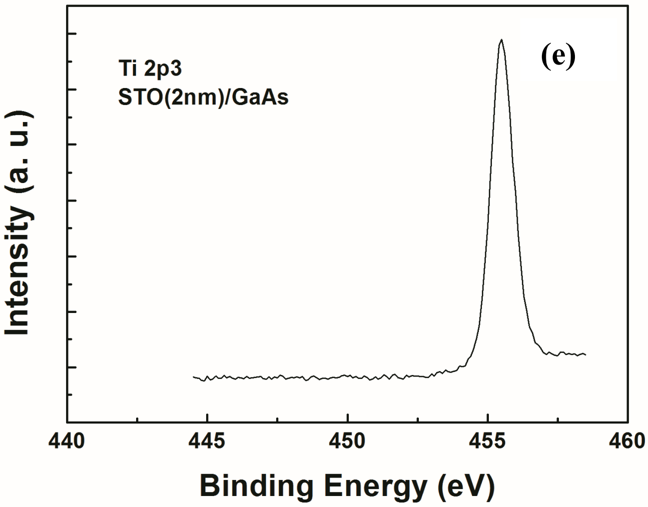
Ti 2p3
STO(2nm)/GaAs
(e)
Intensity (a. u.)
Binding Energy (eV)
440
445
450
455
460

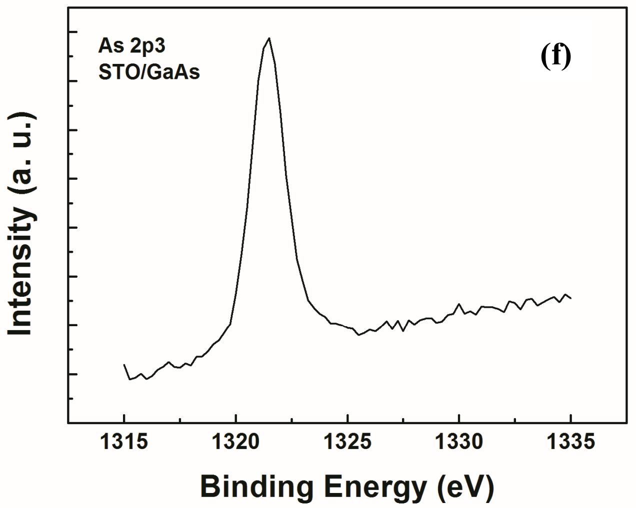

Fig. 3.9 XPS and UPS spectra of STO on GaAs. Core level Ti $2p_{3/2}$ spectra recorded on STO (a) and STO (2 nm)/GaAs (e), As $2p_{3/2}$ spectra on GaAs (c) and STO (2 nm)/GaAs (f).VB spectra for STO (b) and GaAs (d). All VBM values of the samples are calculated by using method of linear extrapolation of the leading edge to the base line.

Fig. 3.9 (a) - (f) exhibit the valence band edges and CL positions of STO thick film, GaAs substrate and STO/GaAs heterostructure, respectively. The VBM and the CL position for the 150 nm thick STO film are 2.1 eV and 457.7 eV (Ti $2p_{3/2}$), and for the clean high resistivity GaAs substrate are 1.3 eV and 1325.5 eV (As $2p_{3/2}$). For the 2 nm thick STO film on high resistivity GaAs heterostructure, the CL positions are 455.5 eV for STO (Ti $2p_{3/2}$) and 1321.5 eV for GaAs (As $2p_{3/2}$). Hence, the separation between As $2p_{3/2}$ and Ti $2p_{3/2}$ for the STO (2 nm)/GaAs is 866.0 eV. Based on the above values, the VBO of STO/GaAs can be calculated to be 2.6 eV. The conduction band offset (CBO) can be obtained by using the formula:

$$\Delta E_c = (E_g^{GaAs} - E_g^{STO}) + \Delta E_v \tag{3.2}$$

where ΔE_c represents CBO, E_g^{GaAs} represents the band gap of GaAs and E_g^{STO} represents the band gap of STO. As the band gaps of STO and GaAs are 3.3 eV and 1.4 eV, respectively [Y. Liang, 2005], we can find the CBO of the heterostructure to be 0.7 eV. Our result is similar to the VBO and CBO values measured from STO/GaAs heterojunction fabricated by molecular beam epitaxy (MBE) technique [Y. Liang, 2005]. The samples of us were fabricated by using LMBE, which had a much larger growth temperature than that of the samples fabricated by MBE. It indicates that the band discontinuities are not much influenced by the growth temperature. Table 3.3 gives the measured values for CL positions and VBMs. As both of VBO and CBO of STO/GaAs are positive numbers, the valence band and conduction band of the film are all lower than that of the substrate, which suggests that STO/GaAs fabricated by LMBE forms a type II heterojuction [Y. Liang, 2005]. The band alignment diagram of the STO/GaAs heterojuction is shown in Fig. 3.10.

Table 3.3. CL positions determined by XPS and VBM values determined by UPS

Sample	State	Binding energy (eV)
STO	Ti $2p_{3/2}$	457.7
	VBM	2.1
GaAs	As $2p_{3/2}$	1325.5
	VBM	1.3
STO/GaAs	Ti $2p_{3/2}$	455.5
	As $2p_{3/2}$	1321.5

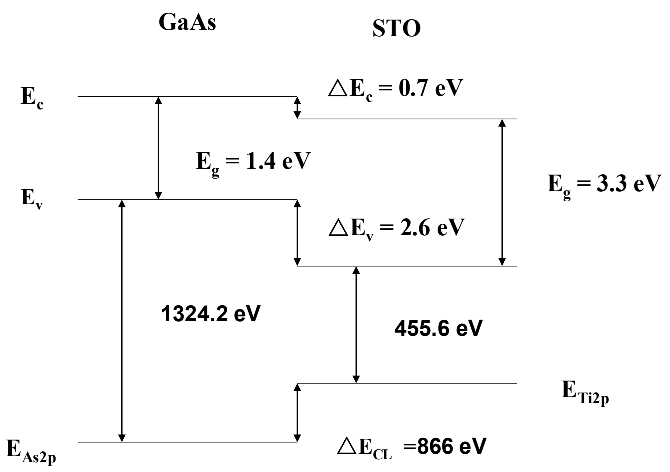

Fig. 3.10 Band alignment diagram of STO/GaAs heterojunction.

3.7 Summary

In this work, epitaxial $Ba_{0.7}Sr_{0.3}TiO_3$ thin films have been successfully grown on GaAs substrates by LMBE with a $SrTiO_3$ buffer layer. The microstructure of the heterostructure was analyzed by X-ray diffraction technique. The Φ scan results measured indicates the in-plane orientation relationship between the thin films and substrates to be [100]BST||[100]STO||[110]GaAs. Atomic force microscopy was used to study the surface morphology of the films. Good crystallinity of the epitaxial STO thin film grown on the GaAs substrate was evident by cross-section TEM. The

XPS measurement confirmed that the composition of the as-grown $Ba_{0.7}Sr_{0.3}TiO_3$ thin films on STO/GaAs is consistent with the stoichiometry, and the chemical valences of Ba, Sr, Ti, and O elements of BST are +2, +2, +4, and -2, respectively. The energy band alignment at STO/GaAs interface was also investigated by using x-ray and ultraviolet photoemission method. A type II heterojunction with a valence band offset of 2.6 eV and conduction band offset of 0.7 eV is formed. The accurate measurement of the energy band of STO/GaAs heterojunction should be important for both fundamental study and the applications of STO/GaAs based devices.

CHAPTER 4

In-plane dielectric and ferroelectric properties of BST/STO/GaAs heterostructure

4.1 Introduction

The dielectric and ferroelectric properties of BST heterostructures are quite attractive these years. However, from the literature study, the samples always measured with the parallel-plate capacitor such as electrode /BST/electrode/substrate. The parallel-plate electrodes are not applied in the commonly used microwave devices such as phase shifters. For the typical microwave devices, the in plane electrodes configuration are commonly used. The configuration of it is like electrode/BST/substrate. Compared with conventional ferroelectric film-based parallel plate capacitors, coplanar capacitors have much lower capacitance values and tunability since the capacitance from the air and substrates are not tunable. The quality of the film can be controlled better for the in plane electrodes than the parallel plate electrodes. Interdigital capacitor (IDC) is one of the most commonly used configurations for the microwave devices application. IDC can be applied in monolithic microwave integrated circuits (MMICs) for conduction, as Hargsoon reported [Y. Hargsoon, 1996]. It can also be used for a component of thin film acoustic electronic transducers [S. Spartak, 1999]. IDC can also be used for the basic dielectric studies for thin film samples [R. Lgreii, 2004]. In this thesis, the electrical properties and ferroelectric properties of our BST film samples are measured by using the IDC electrodes.

In the previous chapter, we have deposit the epitaxial BST thin films on the GaAs substrates with a buffer layer of STO. In this chapter, we will measure the dielectric and ferroelectric properties of the thin film samples produced before. From the equipment measurement, we will get only the pure capacitance values. When we use the IDC electrodes, the dielectric constant can be calculated out by referring to Gevorgian model [S. S. Gevorgian, 1996].

4.2 Electrode Patterning of the (Ba, Sr)TiO$_3$ thin films

Interdigital capacitor (IDC) has several strongpoints beyond other electrodes for microwave device applications, including low capacitance, simple production methods and can deposit on the microwave applications easily. In this section, the details of producing interdigital electrode will be introduced.

4.2.1 Electrode deposition

The magnetron sputtering system is a one of the famous thin film fabrication techniques. It can be used for almost all materials. After the heterostructure of BST/STO/GaAs is prepared, we deposit a thin gold (Au) layer on top surface of the heterostructure as the electrode. The target for deposition can be conducting or non-conducting. It should be noticed that for different materials, the sputtering sources should be selected carefully. For the conducting samples, it usually uses DC sputtering system. For the insulating materials, it should be preventing accumulated of the electric charges. Thus, the target should use a high frequency plasma discharge. Fig. 4.1 shows the photography of the magnetron sputtering used in our laboratory. For our equipment, RF power supply or DC power supply can be selected. To keep the target from too high temperature, a water cooling system is included in the system.

Fig. 4.1 Photograph of magnetron sputtering system.

In this chapter, the gold layer on top surface of the samples was fabricated by the DC magnetron sputtering. Before sputtering, the surface of the BST film samples should be cleaned. Acetone is applied first for the cleaning and then the IPA solution and the deionized water. The whole cleaning process should be done in the ultrasonic bath.

4.2.2 Photolithography

Interdigital capacitor is usually produced by photolithography technique, which is the basic for defining the shape of micro machine structure. The techniques are essentially the same as that used in the microelectronic industry. For a photolithographic process, several steps are involved. Figure 4.2 exhibits the flow charts for the photolithographic technique process.

Table 4.1 Deposition conditions for Au sputtering.

Target material	Gold (Au)
Sputtering power	70 W
Ar gas pressure	1.5 Pa
Gas flow rate of Ar	80 sccm
Deposition time	10 min
Thickness of Au (Measured by surface profiler)	150 nm
Substrate temperature	Room temperature

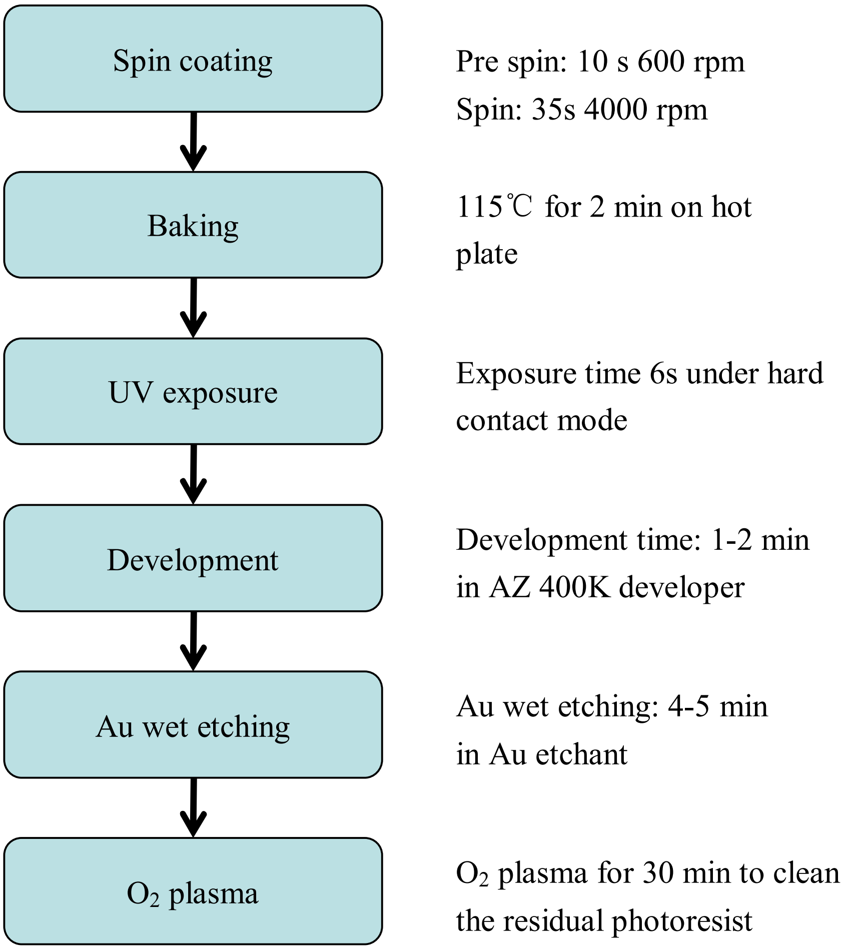

Fig. 4.2 Process flow of the photolithographic technique.

1. Photo masks

Photo masks are one of the most important instruments for micro-patterning of the electrodes for the thin film samples. It should be prepared well before the fabrication. The photo mask used in this work was produced by Microelectronic

Fabrication Facility of Hong Kong University of Science & Technology. We apply AutoCAD to design the electrode patterns on the photo masks. In the photo mask, the smallest distance is around 2μm. If one hopes to make a more accurate photo mask, it can be reached by using single crystal quartz as the mask's material.

2. Photoresists

Photoresist have two categories, which are positive photoresists and negative photoresists. The function of photoresist is that they are easily changed by ultraviolet (UV) light. When the UV light attacks the surface of the positive photoresist, it will make weaker the bonds inside the photoresist. After that, the photoresist developer can decompose the positive photoresist. On the other hand, for the negative photoresist, the parts which are strike by the UV light cannot be dissolved by the photoresist developer as the bonds inside the photoresist are strengthened. Therefore, a negative image of the mask is then transferred to the photoresist.

The sample was first cleaned for 2 min in an ultrasonic bath of acetone, and then rinsed in ethanol to remove particulate matter on the surface as well as any traces of organic, ionic, and metallic impurities. The sample was finally dried in a stream of compressed air. After cleaning, a positive photoresist AZ 5214 was spun coated on the surface of the sample at 4000 rpm for 35 seconds after a 10 seconds pre-spin process at 600 rpm, resulting in an approximately 1.0 -1.2 µm thick uniform layer.

3. Baking process of photoresist

Before receive the UV striking, the samples with photoresist on their top surface should get through a baking process, which could make the photoresist sensitive to the UV light. In this work, the baking process is setting at 115 °C for 2 min. This process will remove most of the solvent, which makes the thickness of the photoresist on top surface of the samples decreasing about 25% [N. Y. Chan, 2010]. Fig. 4.3 shows the spin coating system and baking system used in this work.

Fig. 4.3 Spin coating system (Left) and baking system (Right).

4. Exposure of UV light by means of photolithography

Optical aligner is used for the photolithography technique. It can control the position of the photomask and the samples at the same time. There is a UV light source including in the optical aligner for sample exposure under UV light. Fig. 4.4 shows the photolithography system used in this work (OAI MDL 800 Series, the one inside PolyU class 1000 cleanroom). There are many types of exposure methods. For instance, we will introduce two types of exposure methods for the optical aligner. One is hard contact mode and the other is called proximity mode. For the hard contact mode, we put the photoresist on top surface of the thin film samples to contact with the photomask. The advantages of this exposure are that it can produce a relatively high resolution photolithography patterns. The disadvantage of it is the photomask is contact with the photoresist during the exposure process. Thus it is easily to break or damage the photomask. The photolithography pattern may also be damaged by this contact. While for the proximity mode, we keep a relatively small distance between the samples and the photomask during the exposure process. This distance is usually 10 to 25 microns, which can be automatically controlled by the optical aligner. Due to the existence of this small distance between the photomask and the photoresists, the exposure UV light will be diffracted by this gap. Thus, it will decrease the resolution of the photolithography pattern which cannot be that high as the hard contact mode. However, this method won’t damage the photomask or sample patterns.

In this work, we use the hard contact mode for the higher resolution pattern. It should be paid attention that the photomask contacted with the photoresist surface well. Through the use of aligner, the photoresist layer on the film is exposed to UV light for 6 seconds.

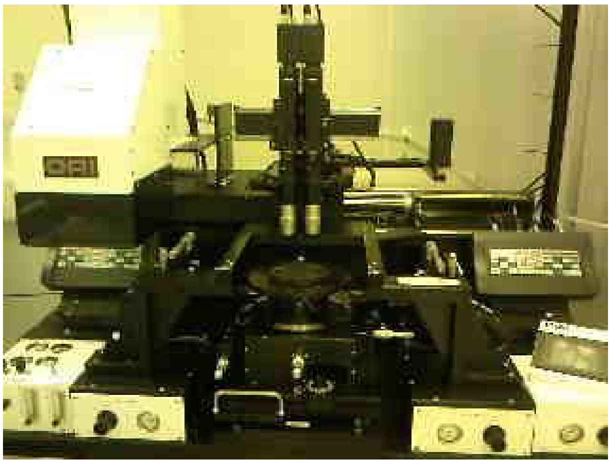

Fig. 4.4 Photo mask aligner (OAI MDL 800 Series).

5. Development and etching

In this work, AZ400K developer with deionized water ratio 1:4 was used to remove the unwanted positive photoresist AZ5214. After the development process, the pattern was formed. A suitable chemical solution was then used to remove the material which was not protected by the photoresist. The chemical used is dependent on the materials. The process of wet chemical etching is to remove material by immersing the wafer in a liquid bath of the chemical etchants. The Au etching solution is prepared by mixing the solution of KI, I_2 and H_2O. During the Au etching process, the thin film samples should be placed fully inside the etching solution. The etching process can be observed by raw eyes. When the required patterns show up clearly and completely, the samples can be taken out from the etchant.

6. Eliminating the remain photoresist by O_2 plasma.

Once the wet etching process is complete, the protective layer of photoresist is removed with O_2 plasma. Plasmas for etching are formed by applying a radio-frequency electric field to a gas held at low pressure in a vacuum chamber. Because the energy of the electron in the plasma is much higher than the chemical bond energy, molecules in the plasma are essentially randomized, breaking down by recombination with electron. Finally, the sample is inspected under an optical microscope. Fig. 4.5 shows picture of the final structure of the sample with an interdigital electrode pattern.

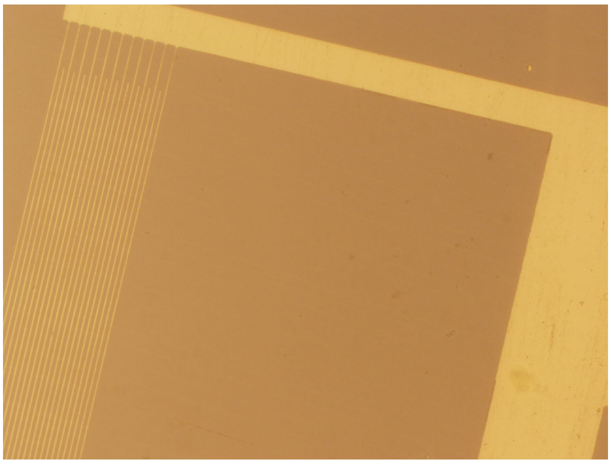

Fig. 4.5 Photography of interdigital electrode pattern.

There are some important parameters in these steps. e.g. UV exposure time and development time. Especially the length of time for the gold etching, it will be over-etched if the time is too long, leading to the partial detachment of the electrode pattern. All the parameters must be well-controlled. Fig. 4.6 exhibits the six procedures for completing the photolithography process.

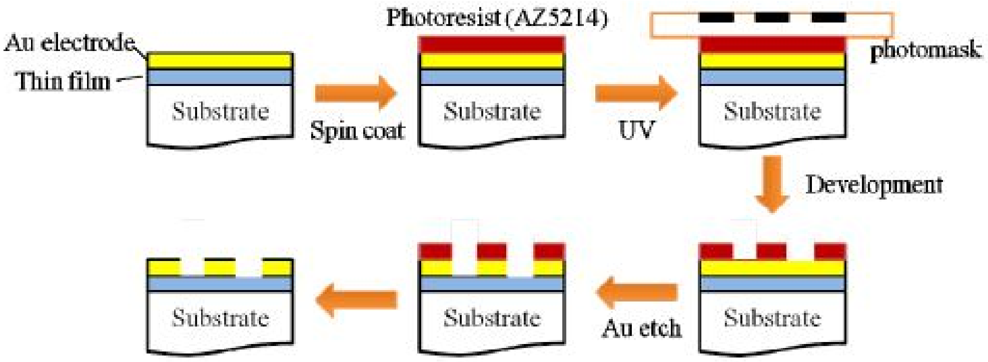

Fig. 4.6 Steps for fabricating pattern by photolithography

7 Wire bonding process

After the interdigital electrode pattern is fabricated successfully by photolithography, the IDC was wire bonded to a piece of printed circuit board (PCB) for easy handling and better electrical contact during subsequent measurement process. Wire bonding is the basic method of making connections between an electronic sample and PCB for electrical device fabrication. Fig. 4.7 shows the picture of the wire bonding machine used in this work. The aluminum (AL) is applied for bonding wires. During the measurement, the conditions for bonding Au/BST/STO/GaAs with PCB board are summarized in Table 4.2.

Fig. 4.7 Wedge bonder (AB 510)

Table 4.2 Conditions for bonding Au/BST/STO/GaAs with PCB board

	Samples	PCB board
Bonding energy	125 J	135 J
Bonding time	45 ms	55 ms
Bonding force	20 g	40 g

4.2.3 IDC geometry

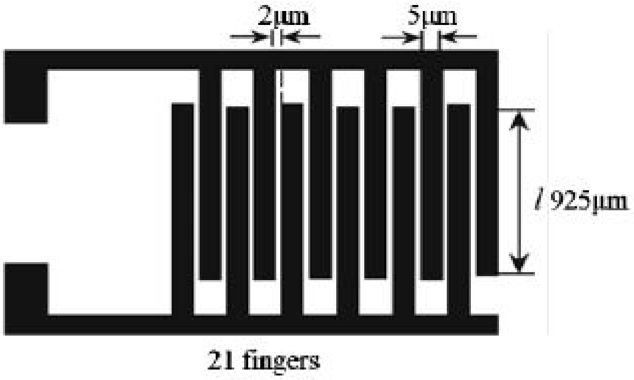

Fig. 4.8 Schematic diagram showing the IDC

In this work, we apply interdigital capacitors (IDC) for dielectric and ferroelectric measurement as shown in Fig. 4.8. A set of geometrical parameters such as the electrode finger “width”, “gap”, “length” and “number” are needed to describe the electrode.

An IDC can be divided into two parts: interdigital electrode “fingers” (the group of parallel lines) and two electrode “arms” with the “pads”. The “fingers” part may be regarded as the “main” interdigital electrodes and the other parts are for the convenience of measurement. The IDC used in this work had a total of 21 fingers with finger length of 925 μm, and finger width of 5 μm. The finger gap spacing with is 2~3 μm.

4.2.4 Extraction of Relative Permittivity of the Film

The sum of partial capacitances can be used to calculate the two layer IDC capacitances. The partial capacitances are calculated by air, substrate and ferroelectric thin films. Fig. 4.9 shows the substrate with two layers for the IDC. ε_1 is used to represent the substrates' relative permittivity. ε_2 is used to represent the ferroelectric layer's relative permittivity. The model should be based on the conditions of $\varepsilon_2 > \varepsilon_1$ and $h_1 > h_2$. C_3 is used to represent the capacitance of the IDC with three fingers. C_n is used to represent the capacitances of IDC with periodical $(n-3)$ fingers structure (shown in Fig.4.9 (c)). C_{end} is used to represent the correction term for the end parts of the strips [Gevorgian, 1996]. For the IDC with finger number $n \geq 3$, the total capacitance C is the sum of the above three items. Therefore, the total capacitance C can be calculated with the equation:

$$C = C_3 + C_n + C_{end} \tag{4.1}$$

According to Gevorgian's model, C_n can be calculated by the equation:

$$C_n = (n-3)\varepsilon_0\varepsilon_{en}\frac{K(k_0)}{K(k_0^{'})}l \tag{4.2}$$

where k_0, $k_0^{'}$ can be calculated by:

$$k_0 = \frac{s}{s+g} \tag{4.3}$$

$$k_0^{'} = \sqrt{(1-k_0^2)} \tag{4.4}$$

where ε_{en} can be calculated by:

$$\varepsilon_{en} = 1 + q_{1n}\frac{\varepsilon_1 - 1}{2} + q_{2n}\frac{\varepsilon_2 - \varepsilon_1}{2} \tag{4.5}$$

where filling factor q_{in} in the above equation can be calculated by:

$$q_{in} = \frac{K(k_{in})}{K(k_{in}^{'})}\frac{K(k_o^{'})}{K(k_0)} \tag{4.6}$$

where k_{in} can be calculated by:

$$k_{in}=\frac{\sinh(\frac{\pi s}{2h_i})}{\sinh(\frac{\pi(s+g)}{2h_i})}\sqrt{\frac{\cosh^2(\frac{\pi(s+g)}{2h_i})+\sinh^2(\frac{\pi(s+g)}{2h_i})}{\cosh^2(\frac{\pi s}{2h_i})+\sinh^2(\frac{\pi(s+g)}{2h_i})}},i=1,2 \tag{4.7}$$

The capacitance of IDC with three fingers C_3 can be calculated by:

$$C_3=4\varepsilon_0\varepsilon_{e3}\frac{K(k_{03}^{'})}{K(k_{03})}l \tag{4.8}$$

where

$$\varepsilon_{e3}=1+q_{13}\frac{\varepsilon_1-1}{2}+q_{23}\frac{\varepsilon_2-\varepsilon_1}{2} \tag{4.9}$$

$$q_{i3}=\frac{K(k_{i3})}{K(k_{i3}^{'})}\frac{K(k_{03}^{'})}{K(k_{03})},i=1,2 \tag{4.10}$$

$$k_{03}=\frac{s}{s+2g}\sqrt{\frac{1-(\frac{s+2g}{3s+2g})^2}{1-(\frac{s}{3s+2g})^2}} \tag{4.11}$$

$$k_{i3}=\frac{\sinh(\frac{\pi s}{2h_i})}{\sinh(\frac{\pi(s+g)}{2h_i})}\sqrt{\frac{1-\frac{\sinh^2(\frac{\pi(s+g)}{2h_i})}{\sinh^2(\frac{\pi(3s+2g)}{2h_i})}}{1-\frac{\sinh^2(\frac{\pi s}{2h_i})}{\sinh^2(\frac{\pi(3s+2g)}{2h_i})}}} \tag{4.12}$$

The end capacitance of the *n* fingers C_{end} can be calculated by:

$$C_{end}=4ns(2+\pi)\varepsilon_0\varepsilon_{end}\frac{K(k_{0end})}{K(k_{0end}^{'})} \tag{4.13}$$

where

$$\varepsilon_{end}=1+q_{1end}\frac{\varepsilon_1-1}{2}+q_{2end}\frac{\varepsilon_2-\varepsilon_1}{2} \tag{4.14}$$

$$k_{0end}=\frac{x}{x+2g_{end}}\sqrt{\frac{1-(\frac{x+2g_{end}}{x+w+2g_{end}})^2}{1-(\frac{x}{x+w+2g_{end}})^2}} \tag{4.15}$$

The penetration depth in the above equations is corresponding to the width of the finger spacing of the IDC. According to our analyze, the ferroelectricity and tunability may have a huge increasing extent when the finger spacing of the IDC decreases. With increasing of the finger spacing, the electric field will penetrate deeper for the low dielectric constant substrate than the high dielectric constant thin film. When the numbers of fingers increase, the dielectric layer covered by the electric field will increase significantly as well. By this reason, number of fingers increasing will result in promotion of the dielectric properties of IDC.

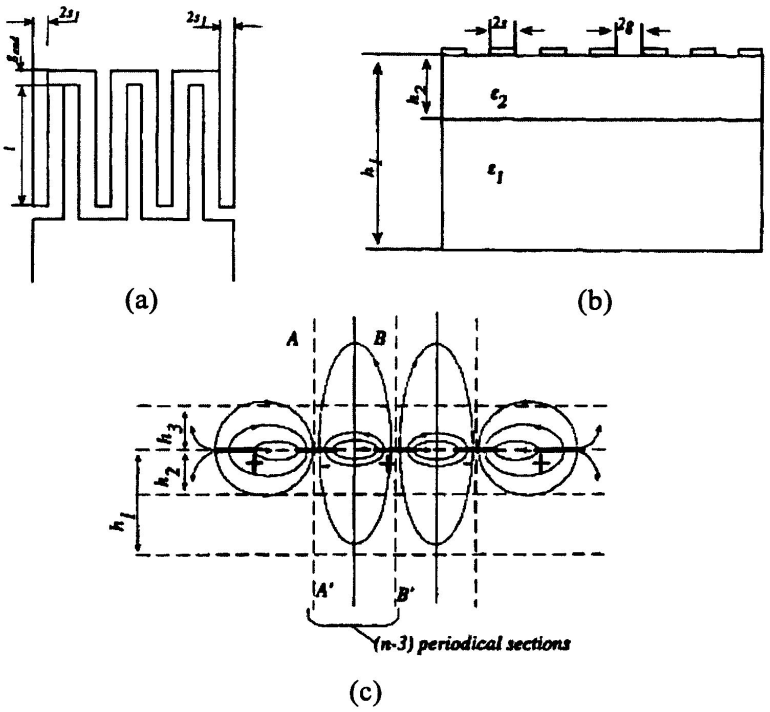

Fig. 4.9 Two layered substrate for the interdigital capacitor (IDC). (a) Layout and (b) cross section of the IDC, and (c) potential distribution and schematics of electric field distribution [Gevorgian, 1996].

4.3 Measurement of Dielectric Constant of (Ba, Sr)TiO$_3$ thin films

4.3.1 Dielectric constant as a function of frequency

The room-temperature dielectric constant ε of the $Ba_{0.7}Sr_{0.3}TiO_3$ thin films as a function of frequency was measured using a HP 4294A precision impedance analyzer (measured frequency range: 1 kHz -10 MHz). Fig. 4.10 shows the variation of dielectric constant of the BST thin film as a function of frequency at room temperature. The relative permittivity of the films decreases with increased frequency. Typical reported dielectric constants of BST films range from ≤ 300 for polycrystalline films [C. Basceri, 1997] to 700 - 3000 for epitaxial films [W. Chang, 1999; C. L. Chen, 1999]. The range of dielectric constant of our results is from 700 – 870 which is consistent with above literature. The dielectric loss of the film was found to be varied throughout the whole measured frequency, and at high frequency, the loss tangent rises rapidly. The loss tangent values are similar to those measured factor-frequency characteristics of BST thin film on bare high-resistivity silicon reported in the literature [H. -S. Kim, 2005].

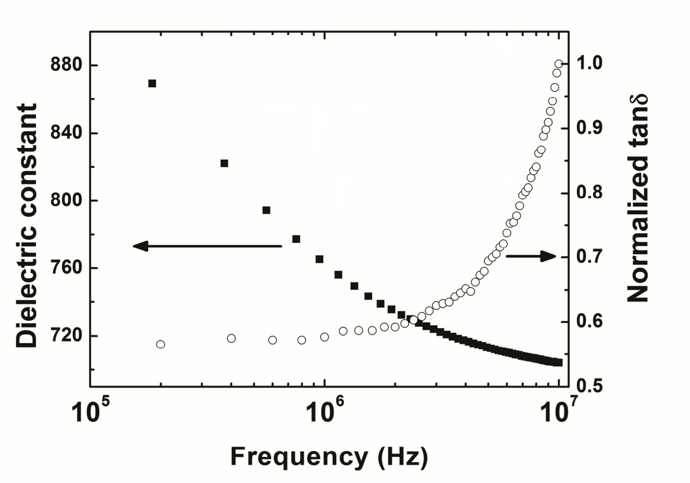

Fig. 4.10 Dielectric constant and normalized loss of 300 nm BST film as a function of frequency at room temperature.

4.3.2 Dielectric constant as a function of temperature

The dielectric constant of the BST thin films as a function of temperature was measured using an HP 4294A impedance analyzer connected to a temperature-controlled chamber (Oxford). Fig. 4.11 shows the temperature-dependent in-plane dielectric constant *ε* of the BST thin film. The measurement was conducted at four different frequencies as 1 kHz, 10 kHz, 100 kHz and 1 MHz. The maximum dielectric constant at these four frequencies was found to be 1100, 980, 900, and 780, respectively. Almost same value of Curie temperature point is demonstrated for these four measuring frequencies, which exhibits from curves at $T_c \approx 52$ °C. The obtained value is about 19 °C higher than that of the bulk BST material ($T_c = 33$ °C). The mechanism of shift in T_c of the BST thin film along the in-plane direction is attributed to the effect of in-plane tensile strain induced by the lattice misfit. The in-plane strain s of the BST thin film can be calculated by using an equation

$s = (a_{||} - a_0) / a_0$, where $a_{||}$ is the lattice parameter of the BST thin film and a_0 is the lattice parameter of bulk BST. Based on the lattice parameters, we calculated from XRD results and the value of s is found to be 0.68%. According to the literature review, the Curie temperature T_c of ferroelectric thin films can be enhanced hundred centidegrees than its inherent value with 1% in-plane tensile strain. The shift in T_c of our BST/STO/GaAs heterostructure is not as significant as expected value. Comparing with the BST thin film grown on MgO (001) single-crystal substrate, whose Curie temperature is 50 °C higher than that of bulk BST with 1.65% in-plane strain, our result is quite small [D. Y. Wang, 2005]. Possible explanations for the difference could be (a) the compressive strain induced by the STO buffer layer is gradually relaxed as the film thickness increases, and (b) the oxygen deficiency in the heterostructure. Another possible cause for shift of Curie temperature might be deviated ratio of Ba/Sr. The corresponding loss tangent data is present in Fig. 4.11. The value of tanδ was found to be dependent on the temperature and frequency ranging from 0.021 to 0.045.

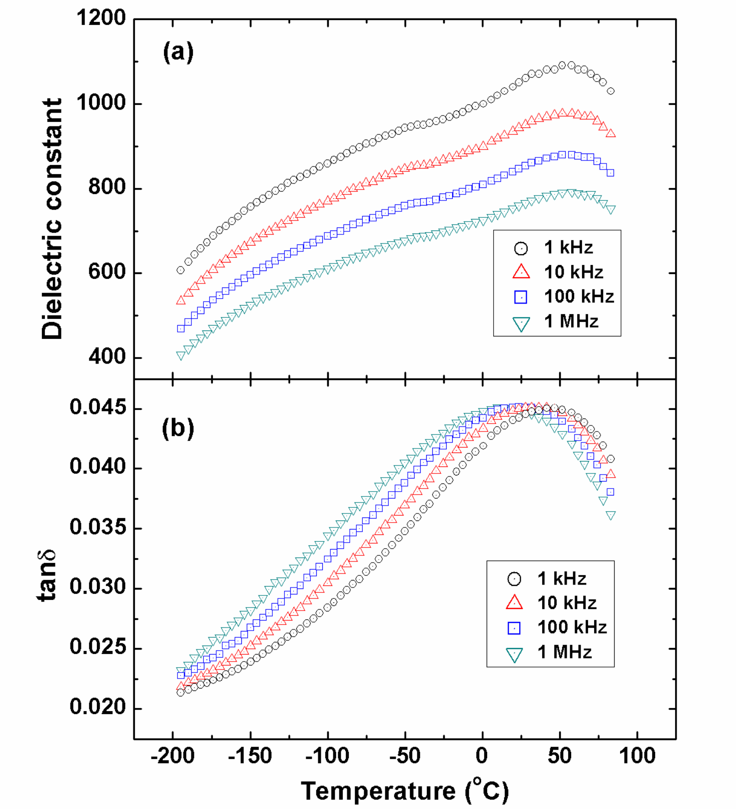

Fig. 4.11 (a) In-plane dielectric constant and (b) dielectric loss of BST thin film as a function of temperature.

4.3.3 Dielectric tunability of the BST thin films

To examine the feasibility of making such novel tunable devices, BST/STO/GaAs can combine the frequency agile electronics of BST with the high-performance microwave capabilities of GaAs. We have measured the electric-field dependence of the dielectric constant and loss for the 300 nm BST film on STO/GaAs. As shown in Fig. 4.12, the heterostructure exhibits a butterfly-shaped ε-E and tan δ-E dependence at room temperature. The electric field E_m at which ε is a maximum is found to be 0.7 V/μm. The maximum in-plane dielectric tunability is calculated to be 30% at 1 MHz under a moderate electric-field of 10 V/μm. The dielectric loss at zero fields is relatively high, which may be explained by the ferroelectric phase induced by the strain [D. Y .Wang, 2005]. The commonly used figure of merit for the quality of frequency and phase agile materials is a simple approach for relating the tunability and dielectric loss in a tunable material, the so-called K factor defined as [X. X. Xi, 2000]:

$$K = \frac{\varepsilon(0) - \varepsilon(E_{\max})}{\varepsilon(0)} \frac{1}{(\tan\delta)_{\max}} \qquad (4.16)$$

where *(tanδ)*$_{msx}$ is the maximum loss under all the applied fields. The *K* factor at room temperature was obtained to be ~8 based on the result in Fig. 4.12. The obtained tunability and *K* factor of our BST films grown on GaAs are lower compared to the reported BST film grown on MgO [D. Y. Wang, 2005]. However, our results are superior to the performance measured from BST film grown on high resistivity Si substrate [H. -S. Kim, 2004].

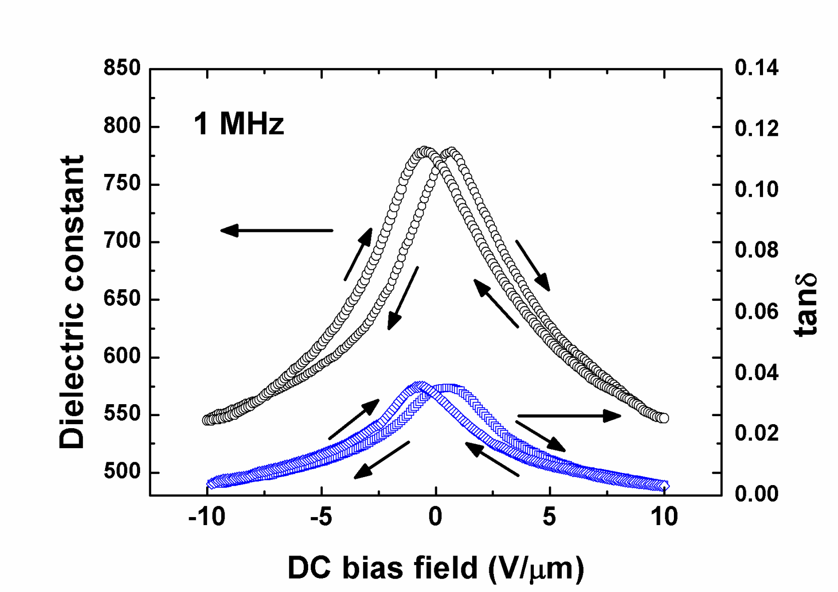

Fig. 4.12 In-plane dielectric constant of BST thin film as a function of electric field at 1 MHz.

4.4 Hysteresis measurements

The polarization-electric field hysteresis loops of the BST/STO/GaAs heterostructure with interdigital capacitors were measured at room temperature. As seen from Fig. 4.13, the BST/STO/GaAs heterostructure exhibits a typical ferroelectric behavior with a remnant polarization (P_r) of 0.5 μC/cm^2 and an electrical coercive field (E_c) of 40 kV/cm. In comparison with BST thin film grown on $MgAl_2O_4$ substrate whose remnant polarization P_r and coercive field E_c were found to be 7.1 μC/cm^2 and 12 kV/cm [X. Y. Zhou, 2006], our results exhibit a weak ferroelectricity along the in-plane direction. The weak ferroelectricity may be explained by the oxygen deficiency leading to higher leakage current in the heteostructure.

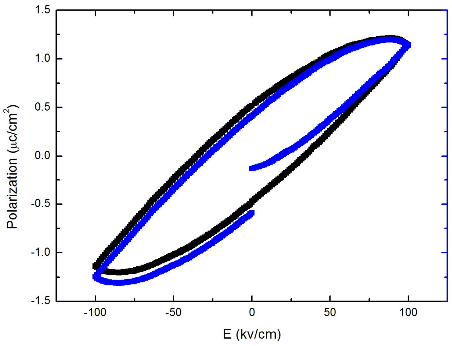

Fig. 4.13 P - E loops of the BST/STO/GaAs heterostructure.

4.5 Summary

To summarize, we have investigated the dielectric and ferroelectric properties of BST thin films epitaxially grown on high resistivity GaAs substrate with a STO buffer layer. The interdigital capacitor was applied to test the in-plane dielectric properties of BST thin films. Standard photolithography was employed to make the IDC with 100-nm thick Au top layer. According to our results, the dielectric constant of the BST film decreases with the increased frequency. Curie temperature point of BST thin film shifts to around 19 °C higher than that of BST bulk material. Butterfly-shaped C-V characteristic curves were observed. A relatively large dielectric tunability of 30% was found at 1 MHz.

CHAPTER 5

Conclusions and suggestions for future work

5.1 Conclusions

The present research work is on the heteroepitaxy and investigation of the structural and dielectric properties of epitaxial perovskite titanate thin films grown on III-V semiconductor GaAs wafer. Our results offer the possibility to combine frequency agile electronics of ferroelectric titanate with the high-performance microwave capabilities of GaAs for room temperature tunable device application. The main conclusions are summarized as follows:

1. High quality epitaxial Ba0.7Sr0.3TiO3 (BST) thin films were deposited on GaAs substrates with STO buffer layer by using laser molecular beam epitaxy (L- MBE) technique. The L-MBE technique provides a convenient way of growing oxide thin films under relatively high oxygen pressure, enabling atomic control and

characterization of thin film growth process. The optimized deposition process has been obtained.

2. Microstructures of the thin film were studied by X-ray diffraction technique, which confirms single orientation (00l) of grown BST thin films. The in-plane orientation relationship between the deposited BST film and GaAs substrate is [100]BST||[100]STO||[110]GaAs, which means a 45°in-plane rotation of BST with respect to GaAs exist. The surface morphology of BST on GaAs was investigated by AFM, showing a smooth surface with a relatively small root-mean square roughness value of 1.60 nm. Such good surface makes the thin film suitable for fabricating devices with in-plane electrodes.

3. The interface structure of STO/GaAs was studied by transmission electron microscopy (TEM). The STO film shows good crystallinity and has an in-plane film-substrate orientation relationship of [100] STO|| [110] GaAs. The chemical valences of BST thin films on STO/GaAs and energy band at the interface of STO/GaAs were investigated using photoelectron spectroscopy. Based on the

results, a type II heterojunction with a valence band offset of 2.5 eV and conduction band offset of 0.7 eV is formed.

4. The dielectric properties were also studied. The interdigital electrodes were used for dielectric measurement, which were fabricated by Au sputtering and photolithography. Curie temperature point of BST thin film shifts to around 19 ℃ higher than that of BST bulk material. The mechanism of shift in Tc of the BST thin film along the in-plane direction is attributed to the effect of in-plane tensile strain induced by the lattice misfit. Our results show that the Curie temperature is near the room temperature and the loss tangent is low, which make them suitable for microwave devices.

5. The electric-field dependence of the dielectric constant and loss for the 300 nm BST film on STO/GaAs was also examined. Butterfly-shaped ε-E and tan δ-E dependence are observed. The maximum in-plane dielectric tenability is found to be 30% at 1MHz under a moderate electric-field of 10 V/μm. The figure of merit K at room temperature is obtained to be around 8. The obtained tunability and K factor of our BST films grown on GaAs are lower compared to the reported BST

film grown on MgO. However, our results are superior to the performance measured from BST film grown on high resistivity Si substrate, suggesting that it is a promising candidate for tunable microwave applications.

5.2 Suggestions for future Work

This thesis was devoted to study several aspects of BST thin films integrated with GaAs substrates. The BST/STO/GaAs will be one of the potential materials for fabricating the microwave device application. In the following section, some recommendations will be provided for the future work of the basic research, which can be realized as the spread of the present work of the thesis.

1. The integration of BST thin film with semiconductors attracts a lot of research interests for high frequency microwave device applications. Therefore, studying the high frequency dielectric and ferroelectric properties of the BST heterostructures will be one of the important future works. The microwave devices such as phase shifters based on integration of BST film on GaAs

substrate can be considered based on the work done in this thesis. By considering GaAs wafer with high-performance microwave capabilities and large-size availability, the perovskite titanate/III-V semiconductor heterostructure is very promising to be a new system for tunable microwave applications.

2. In order to put the interesting material into practical applications, the structure to property relationship is quite important to study. Up to now, STO/GaAs and BST/STO/GaAs heterostructures have been successfully fabricated by LMBE. The lattice strain influence and interface effect on the structural and electrical properties have also been studied. However, there are other important factors playing an important role to determine the dielectric and ferroelectric properties, i.e., grain size effect, doping effect, orientation effect and so on.

REFERENCES

[1] A. Tombak, J. P. Maria, F. Ayguavives, Z. Jin, G. T. Stauf, A. I. Kingon, and A. Mortazawi, *IEEE Microw. Wirel. Compon. Lett*. **12**, 3 (2002).

[2] A. Baumert, L. -H. Chang, A. T. Matsuda, T. -L. Tsai, and C. J. Tracy, *J. Appl. Phys.* **82**, 2558 (1997).

[3] A. K. Pradhan, S. Mohanty, K. Zhang, J. B. Dadson, E. M. Jackson, D. Hunter, R. R. Rakhimov, G. B. Loutts, J. Zhang, and D. J. Sellmyer, *Appl. Phys. Lett.* **86**, 012503 (2005).

[4] Acikel, T. R. Taylor, P. J. Hansen, J. S. Speck, and R. A. York, *IEEE Microw. Wirel. Compon. Lett.* **12**, 7 (2002).

[5] Bailey, A. E, *Electronic materials and processes handbook.* 3rd ed. New York, McGraw-Hill**,** (2003).

[6] Bhalla, A. S., Guo, R. and Roy, R. *Mater. Res. Innov.* **4**, 3 (2000).

[7] B. H. Park, E. J. Peterson, Q. X. Jia, J. Lee and X. Zeng, *Appl. Phys. Lett.* **78**, 533 (2001)

[8] B. M. Kim, T. Brintlinger, E. Cobas, M. S. Fuhrer, H. Zheng, Z. Yu, R. Droopad, J. Ramdani, and K. Eisenbeiser, *Appl. Phys. Lett.* **84**, 1946 (2004)

[9] Basceri, S. K. Streiffer, A. I. Kingon, and R. Waser, *J. Appl. Phys.* **82**, 2497 (1997).

[10] C. D. Wagner, W. M. Riggs, L. E. Davis and G. E. Muilenberg, *A Reference Book of Standard Data for Use in X-Ray Photoelectron Spectroscopy*, USA, Perkin-Elemer Corporation and Physical Electronics Divison, (1979)

[11] C. J. Först, C. R. Ashman, K. Schwarz, and P. E. Blöchi, *Nature* **427**, 53 (2004)

[12] C. Nordling, E. Sokolowski and K. Siegbahn, *Phys. Rev.* **105**, 1676 (1957).

[13] C. L. Chen, H. H. Feng, Z. Zhang, A. Brazdeikis, Z. J. Huang, W. K. Chu, C. W. Chu, F. A. Miranda, F. W. Van Keuls, R. R. Romanofsky, and Y. Liou, *Appl. Phys. Lett.* **75**, 412 (1999).

[14] C. L. Chen, J. Shen, S. Y. Chen, G. P. Luo, C. W. Chu, F. A. Miranda, F. W. Van Keuls, J. C. Jiang, E. I. Meletis, and H. Chang, *Appl. Phys. Lett.* **78**, 652 (2001).

[15] C. M. Carlson, T. V. Rivkin, P. A. Parilla, J. D. Perkins, and D. S. Ginley, *Appl. Phys. Lett.* **76**, 1920 (2000).

[16] C. T. Black and J. J. Welser, *IEEE Trans. Electr. Dev.* **46**, 776 (1999).

[17] C. W. Wilmsen, *Physics and Chemistry of III-V Compound Semiconductor Interfaces,* Plenum Press, New York, (1985)

[18] C. Zhou, and D. M. Newns, *J. Appl. Phys.* **82**, 3081 (1997).

[19] Damjanovic, *Rep. Prog. Phys.* **61**, 1267 (1998)

[20] David E. Fulkerson, *IEEE Trans. Electr. Dev.* **39**, 745 (1992)

[21] D. J. Gao, D. Q. Xiao, J. Bi, P. Yu, G. L. Yu, W. Zhang and J. G. Zhu, *Mater. Trans.* **44**, 1320 (2003).

[22] D. M. Tahan, A. Safari, L. C. Klein, *J. Am. Ceram. Soc.* **79**, 1593 (1996).

[23] D. Y. Wang, Y. Wang, X. Y. Zhou, H. L. W. Chan, and C. L. Choy, *Appl. Phys. Lett.* **86**, 212904 (2005).

[24] E.G. Kostsov, and V. K. Malinovsky, *Ferroelectrics* **94,** 457 (1989).

[25] England, P., Venkatesan, T., Wu, X. D. and Inam, *Phys. Rev. B.* **38**, 7125 (1988).

[26] F. Jona, G. Shirane, *Ferrolectric crystals*. Pergamon Press. Oxford, (1962).

[27] Feng, L. M., Jiang, L. Q., Zhu, M., Liu, H. B., Zhou, X. and Li, C. H., *J. Phys. Chem. Sol.* **69,** 967 (2008).

[28] Glazer, A. *Acta Cryst. B.* **28,** 3384 (1972).

[29] G. D. Wilk, R. M. Wallance, J. M. Anthony, *J. Appl. Phys.* **87**, 484 (2000)

[30] H. Landolt and R. Bornstein, *Ferroelectrics and related substances: A, Oxides*, Springer-Verlag, New York (1981).

[31] H. Landolt, Landolt-Börnstein, *Ferroelectrics and Related Substances, New Series, Group III*, Springer-Verlag, Berlin, (2002).

[32] H. Meuller, N. A. Suvorova, A. Irene, O. Auciello, and J. A. Schultz, *Appl. Phys. Lett.* **80**, 3796 (2002).

[33] H. Li, X. Hu, Y. Wei, Z. Yu, X. Zhang, R. Droopad, A. A. Demkov, J. Edwards, Jr., K. Moore, W. Ooms, J. Kulik, and P. Fejes, *J. Appl. Phys.* **93**, 4521 (2003).

[34] H.-J. Gao, C. L. Chen, B. Rafferty, S. J. Pennycook, G. P. Luo, and C. W. Chu, *Appl. Phys. Lett.* **75**, 2542 (1999).

[35] H.-S. Kim, H.-G. Kim, I.-D. Kim, K.-B. Kim, and J.-C. Lee, *Appl. Phys. Lett.* **87**, 212903 (2005).

[36] H. Yoon, J. K. Abraham, and V. K. Varadan, *Microw. Opt Techn. Let.* **40**, 20 (2004).

[37] I. -D. Kim, H. L. Tuller, H. -S. Kim, J. -S. Park, *Appl. Phys. Lett.* **85,** 4705 (2004).

[38] Vrejoiu, M. Alexe, D. Hesse, and U. Gosele, *Adv. Funct. Mater.* **18**, 3892 (2008).

[39] J. C. Le Breton, S. Le Gall, G. Jézéquel, B. Lépine, P. Schieffer, and P. Turban, *Appl. Phys. Lett.* **91**,172112 (2007).

[40] J. H. Hao, J. Gao, Z. Wang, and D. P. Yu, *Appl. Phys. Lett*. **87**, 131908 (2005).

[41] J. H. Hao, X. T. Zeng, and H. K. Wong, *J. Appl. Phys.* **79**, 1810 (1996).

[42] J. L. Li, J. H. Hao, Y.R. Li , *Appl. Phys. Lett.* **91**, 131902 (2007).

[43] J. S. Wu, C. L. Jia, K. Urban, J. H. Hao, and X. X. Xi, *J. Mater. Res.* **16**, 3443 (2001).

[44] J. Zhang, J. Wang, J. Jiang, et al. *Thin Sol. Films.* **515**, 7721 (2007)

[45] K. B. Kim, T. S. Yun, J. C. Lee, et al. *Micro. Opt. Techni. Lett.* **49**, 2144 (2007)

[46] K. D. Choquette, K. M. Geib, C. I. H. Ashby, R. D. Twesten, O. Blum, H.Q. Hou, D. M. Follstaedt, B. E. Hammons, D. Mathes, R. Hull, *IEEE J. Sel. Top. Quantum Electron.* **3**, 916 (1997).

[47] K. Natori, D. Otani, and N. Sano, *Appl. Phys. Lett.* **73**, 632 (1998).

[48] L. A. Knauss, J. M. Pond, J. S. Horwitz, D. B. Chrisey, C. H. Mueller, *Appl. Phys. Lett.* **69**, 25 (1996).

[49] Li, C., Soh, K. C. K. and Wu, P., *J. Alloys Compd.* **372**, 40 (2004).

[50] M. Hale, S. I. Yi, J. Z. Sexton, A. C. Kummel, and M. Passlack, *J. Chem. Phys.* **119**, 6719 (2003).

[51] M. E. Lines, and A. M. Glass, *Principles and applications of ferroelectrics and related materials.* Oxford University Press. Oxford, (1977).

[52] Mauricio E. Pilleux, Carlos R. Grahann, and Victor M. Fuenzalida: *J. Am. Ceram. Soc.* **6**, 1602 (1994).

[53] M. Hawley, I. D. Raistrick, J. G. Beery, and R. J. Houlton, *Science* **251,** 1587 (1991).

[54] M. Hong, J. Kwo, A. R. Kortan, J. P. Mannaerts, A. M. Sergent, *Science* **283,** 1897 (1999).

[55] Moulson, A. J. and Herbert, J. M. Herbert, *Electroceramics: Materials, Properties, Applications*, West Sussex, John Wiley & Sons Ltd, U.K. (2003)

[56] M. Passlack, J. Abrokwah, R. Droopad, Z. Yu, C. Overgaard, S. Yi, M. Hale, J. Sexton, A. Kummel, *IEEE Electron Dev. Lett.* **23**, 508 (2002).

[57] M. Passlack, M. Hong, and J. P. Mannaerts, *Appl. Phys. Lett.* **68**, 1099 (1996).

[58] Morris, V. J. Kirby, A. R. and Gunning, A. P. *Atomic Force Microscopy for Biologists.* Imperial College Press, London (1999).

[59] M. W. Cole, C. Hubbard, E. Ngo, M. Ervin, M. Wood, and R. G. Geyer, *J. Appl. Phys.* **92**, 475 (2002).

[60] M. W. Cole, P. C. Joshi, M. Wood, and R. L. Pfeffer, *J. Appl. Phys.* **92**, 3967 (2002).

[61] M. W. Cole, W. D. Nothwang, C. Hubbard, E. Ngo, and M. Ervin, *J. Appl. Phys.* **93**, 11 (2003)

[62] N. K. Pervez, P. J. Hansen, and R. A. York, *Appl. Phys. Lett.* **85**, 4451 (2004)

[63] Nath, J., Ghosh, D., Maria, J. P., Steer, M. B., Kingon, A. and Stauf, G. T. *Microwave properties of BST thin film interdigital capacitors on low cost alumina substrates.34th European Microwave Conference,* PP: 1470-1500 (2004).

[64] Q. X. Jia, B. H. Park, B. J. Gibbons, J. Y. Huang, and P. Lu, *Appl. Phys. Lett.* **81**, 114 (2002).

[65] R. A. Mckee, F. J. Walker, M. F. Chisholm, *Phys. Rev. Lett.* **81**, 3014 (1998).

[66] R. Chau, *IEEE Trans. Nanotechnol.* **4**, 153 (2005).

[67] Ramsey, G. H. A. J. B. *Appl. opt.* **8,** 1115 (1969).

[68] Richerson, D. W. Dielectric, magnetic, and optical behavior. *Modern Ceramic Engineering: properties, processing, and use in design.* 3rd ed. Boca Raton, FL CRC Taylor & Francis, 2006

[69] R. Igreji, C. J. Dias, *Sens. Actuators, A* **112**, 291 (2004).

[70] S. E. Moon, E.-K. Kim, M.-H. Kwak, H.-C. Ryu, and Y.-T. Kim, *Appl. Phys. Lett.* **83**, 2166 (2003).

[71] Smith, H. M. and Turner, A. F., *Appl. Opt.* **4,** 147 (1969).

[72] S. Migita and S. Sakai, *J. Appl. Phys.* **89**, 5421(2001)

[73] Sengupta and S. Sengupta, *Mater. Res. Innov.* **2**, 278 (1999).

[74] S. S. Gevorgian, T. Matinsson, P. L. J. Linner, and E. L. Kollberg, *IEEE Trans. Microwave Theory Tech.* **44**, 896 (1996).

[75] S. S. Gevorgian, E. F. Carlsson, S. Rudner, U. Helmersson, E. L. Kollberg, E. Wikborg and O. G. Vendik, *IEEE Trans. Appl. Superconduct.* **7**, 2458 (1997).

[76] Swartz, S. L. *IEEE Trans. Electr. Insul.* **25,** 935 (1990).

[77] T. E. Murphy, D. Chen, J. D. Phillips, *Appl. Phys. Lett.* **85**, 3208 (2004).

[78] T. Horikawa, N. Mikami, T. Makita, J. Tanimura, M. Kataoka, K. Sato and M. Nunoshita, *Jpn. J. Appl. Phys.* **32**, 4126 (1993).

[79] T. Y. Tseng, *Ferroelectrics* **232**, 1 (1999).

[80] T. Yajima, Y. Hikita, and H. Y. Hwang, *Nature Mater.* **10**, 198 (2011).

[81] Von Jurij Šilc, Borut Robič, Theo Ungerer. *Processor architecture: from dataflow to superscalar and beyond*. Springer. (1999).

[82] W. Chang, J. S. Horwitz, A. C. Carter, J. M. Pond, S. W. Kirchoefer, C. M. Gilmore, and D. B. Chrisey, *Appl. Phys. Lett.* **74**, 1033 (1999).

[83] W. Huang, Z. P. Wu, and J. H. Hao, *Appl. Phys. Lett.* **94**, 032905 (2009).

[84] W. Huang, J. Y. Dai, and J. H. Hao, *Appl. Phys. Lett.* **97**, 162905 (2010).

[85] X. X. Xi, H. C. Li, W. Si, A. A. Sirenko, I. A. Akimov, J. R. Fox, A. M. Clark, and J. H. Hao, *J. Electroceram*. **4**, 393 (2000).

[86] X. Y. Zhou, T. Heindl, G. K. Pang, J. Miao, and R. K. Zheng, *Appl. Phys. Lett.* **89**, 232906 (2006).

[87] X. Y. Zhou, D.Y. Wang, L. X. He, Y. Li, Y. Wang, H. L. W. Chan, and C. L. Choy, *Integr. Ferroelectr.* **77**, 157 (2006).

[88] Y. Gim, T. Hudson, Y. Fan, C. Kwon, A. T. Findikoglu, *Appl. Phys. Lett.* **77,** 1200 (2000).

[89] Y. Liang, J. Kulik, T. C. Eschrich, R. Droopad, Z. Yu, P. Maniar, *Appl. Phys. Lett.* **85**, 1217 (2004).

[90] Y. Liang, J. Curless, and D. McCready, *Appl. Phys. Lett.* **86**, 082905 (2005)

[91] Y. Lin, J.-S. Lee, H. Wang, Y. Li, S. R. Foltyn, Q. X. Jia, G. E. Collis, A. K. Burrell, and T. M. McCleskey, *Appl. Phys. Lett*. **85**, 5007 (2004).

[92] Y. Wang, Y. L. Cheng, K. C. Cheng, H. L. W. Chan, and C. L. Choy, *Appl. Phys. Lett.* **85**, 1580 (2004).

[93] Z. P. Wu, W. Huang, K. H. Wong, and J. H. Hao, *J. Appl. Phys.* **104**, 054103 (2008).